Geosci. Instrum. Method. Data Syst. Discuss., 3, 753–823, 2013
www.geosci-instrum-method-data-syst-discuss.net/3/753/2013/
doi:10.5194/gid-3-753-2013

Geoscientific Instrumentation Methods and Data Systems Discussions
Open Access

Auroral spectral estimation with wide-band color mosaic CCDs

B. J. Jackel[1], C. Unick[1], M. T. Syrjäsuo[2], N. Partamies[3], J. A. Wild[4], E. E. Woodfield[5], I. McWhirter[6], E. Kendall[7], and E. Spanswick[1]

[1]Physics and Astronomy Department, University of Calgary, Calgary, Canada
[2]School of Electrical Engineering, Aalto University, Aalto, Finland
[3]Finnish Meteorological Institute, Helsinki, Finland
[4]Department of Physics, Lancaster University, Lancaster, UK
[5]British Antarctic Survey, Cambridge, UK
[6]Department of Physics and Astronomy, University College London, London, UK
[7]SRI International, Menlo Park, California, USA

Received: 3 November 2013 – Accepted: 25 November 2013 – Published: 23 December 2013

Correspondence to: B. J. Jackel (bjackel@ucalgary.ca)

Published by Copernicus Publications on behalf of the European Geosciences Union.

Abstract

Color mosaic CCDs use a matrix of different wide-band micro-filters in order to produce images with several (often three) color channels. These devices are increasingly employed in auroral studies to provide time sequences of two dimensional luminosity maps, but the color information is typically only used for qualitative analysis. In this study we use Backus–Gilbert linear inversion techniques to obtain quantitative measures of effective spectral resolution for multi-channel color mosaic CCDs. These techniques also allow us to explore the possibility of further improvements by modifying or combining multiple detectors. We consider two spectrally calibrated commercial color CCDs (Sony ICX285AQ and ICX429AKL) in order to determine effective wavelength resolution of each device individually, together, and with additional filters. From these results we develop methods to enhance the utility of existing data sets, and propose ways to improve the next generation of low-cost color auroral imaging systems.

1 Introduction

Visible aurora is produced when energetic charges from outer space collisionally excite atmospheric atoms and molecules. These charges tend to move along magnetic field lines connecting the upper atmosphere to more distant regions of the magnetosphere or solar wind. Consequently, observing the spatial distribution and temporal variation of aurora can provide important information about geospace topology and dynamics.

Additional details about source population energy distributions may be obtained if optical observations are spectroscopically resolved. Emitted photon wavelengths can have a complicated dependence on atmospheric composition and density, but certain combinations of emissions may be used to make useful inferences about the precipitation energy (Rees and Luckey, 1974; Strickland et al., 1989). A list of the most commonly studied auroral emissions is included in Table 1, and will be referred to throughout this study.

GID
3, 753–823, 2013

An example synthetic auroral spectrum is shown in Fig. 1. This was produced by simulating the effects of a monoenergetic 1 keV electron beam incident on a realistic atmospheric model (Strickland et al., 1999). The results are highly dependent on incident energy, with higher energies penetrating to lower altitudes and exciting different atmospheric constituents than at higher altitudes. Real precipitation distributions are often quasi-Maxwellian, but the characteristic and total energies can vary considerably as a function of time and location. In Sect. 2.3 we show one example of drastic variations in broad-band auroral intensity over 1 h; similar changes can occur on time-scales of a few seconds or less.

In addition to the possibility of rapid changes in auroral spectral features, there are often also significant "background" contributions such as stars or cloud-scattered moonlight. The background spectrum is typically more of a continuum, so that useful estimates can be obtained from measurements adjacent to auroral emission lines. Errors in background subtraction can be a major concern when attempting spectroscopy with faint auroral emissions.

The disparate requirements of spatially resolved rapid low-light spectroscopy over a wide field of view cannot be achieved with any single instrument. Many auroral observatories use several different devices with complementary capabilities to acquire multiple data streams which may be combined to quantify auroral structure as a function of space, time, and wavelength.

One widely used class of auroral instruments is referred to as wide-field or all-sky imagers (ASIs). These devices use "fish-eye" optics to simultaneously observe most or all of the visible sky. Early versions used photographic plates or film to record images; modern systems use digital array detectors such as charge-coupled devices (CCDs). These detectors typically have a very broad spectral response which includes the entire range of visible wavelengths and may extend well into the infra-red. The resulting "white-light" images include contributions from a wide range of photon wavelengths and are useful for rapid observations or detection of faint aurora.

GID
3, 753–823, 2013

ASIs can be used for quantitative spectroscopy by adding a narrow-band (i.e. 1–2 nm) interference filter to isolate specific emission features. This drastically reduces total photon flux reaching the detector, requiring the use of expensive image intensifier or electron multiplier technology to achieve acceptable levels of signal-to-noise (SNR) even with longer integration times. A "filter-wheel" (typically with 4–8 filters) can be used to cycle between different passbands in order to observe multiple auroral emissions and appropriate background channels. However, a sequence of long-duration exposures through multiple filters inevitably results in a lack of simultaneity that can be highly problematic when observing aurora that varies rapidly in time. One partial workaround involves the use of two or more identical cameras which can measure different emissions at the same time (Steele and Cogger, 1996; Dahlgren et al., 2008). This approach requires careful calibration to quantify any differences in camera response, but the primary disadvantage is the doubling in cost of an already expensive system.

Consumer-grade color cameras have become ubiquitous in recent years. Most of these devices use CCDs with a wide-band micro-filter mosaic overlay. Each individual image pixel receives light from a different portion of the optical spectrum (e.g. red, green, *or* blue); results from neighboring pixels with different filters are interpolated to estimate color (e.g. red, green, *and* blue) at each pixel location. This process involves simultaneous exposure of all pixels, so temporal offsets between color channels is not a problem. Filter rejection will reduce the response relative to a comparable white-light system, but count rates are still high enough that expensive amplification technology is not essential. While early versions of this class of detectors were clearly inferior to scientific grade CCDs, recent products provide high quantum efficiency, low noise, and good uniformity.

Color mosaic all-sky imaging systems are increasingly widely used for auroral observations (e.g. Toyomasu et al., 2008). However, most results are typically only used in a qualitative fashion as summary data products or for public outreach purposes. It is undoubtedly useful to have visually appealing images that faithfully reflect the ap-

GID
3, 753–823, 2013

pearance of aurora as seen by the human eye. It would be beneficial if wide-band color image data could also be used more quantitatively for scientific applications.

To the best of our knowledge, the auroral science literature on this topic is quite limited. Partamies et al. (2007) presented a comparison of wide-band color mosaic imager and narrow-band photometer observations, Sigernes et al. (2008, 2009) provide absolute spectral calibration of several different DSLR cameras, and Partamies et al. (2012) apply tomography to color mosaic images.

More generally, RGB cameras have been used in combination with multiple color filters to estimate daylight and florescent spectra (Nieves et al., 2005, 2007). However, these studies have focused on spectra that are dominated by broad features and it is not clear how their techniques would perform for multiple discrete features such as are typically found in the aurora. More importantly, they do not consider issues regarding non-simultaneous multi-channel measurements of time varying sources.

Low cost auroral imaging

Photographic plates and film were the sole method of recording auroral luminosity for more than a century of observations. The introduction of electronic image sensors, such as CCDs, was a revolutionary development that greatly facilitated data acquisition and analysis. However, early CCDs were extremely expensive. Prices for cutting-edge "scientific-grade" devices remained very high for several decades, and even today it is easy to pay many thousands of dollars for a single high quality CCD. Equally expensive cooling and electronics are required to achieve maximum performance of the costly CCD in a camera. Such an expensive camera naturally deserves the purchase of the best possible all-sky optics, which are inevitably accompanied by custom orders for several large-aperture narrow-band interference filters. As a result, the total cost of a complete state-of-the art auroral imaging system can easily be on the order of 100 000 USD.

While the performance of high end CCDs continues to improve, it is important to recognize that low-cost mass-produced devices are now at a level which would have

GID
3, 753–823, 2013

been called “scientific-grade” only a few years ago. The proliferation of cameras in consumer electronics means that $100 will purchase a high-quantum efficiency low-noise mega-pixel sensor, and prices are falling fast. While very capable, a cheaper CCD only merits similarly inexpensive cooling, electronics, and optics. Consequently, a few thousand dollars is currently sufficient to produce an extremely useful all-sky auroral imaging system.

Significantly lower costs could be reached in return for modest reductions in performance, but at this level ancillary expenses are often more important. Auroral observations usually involve extended operation in polar regions and costly travel to field sites with limited infrastructure. It is not generally worth allocating the engineering resources to save a thousand dollars on instrumentation if operating expenses are several times greater.

To the best of our knowledge, the first large-scale deployment of low-cost auroral imaging systems was as part of the THEMIS ground-based observatory (Donovan et al., 2006; Harris et al., 2008). This project operates “white-light” all-sky imagers at 20 remote field sites in northern Canada and Alaska. Cameras were purchased from a vendor (Starlight-Xpress) who primarily serves the amateur astronomy community. Their camera systems combine thermoelectric cooling and image readout electronics in a convenient package with USB interface. Software drivers are provided for Windows and Linux operating systems. THEMIS GBO systems use single-channel Starlight-Xpress MX716 (now re-branded as “Lodestar”) cameras with additional all-sky optics. The Sony ICX249AL CCD in these systems has a very broad spectral response spanning the entire visible range of wavelengths, so an additional “hot mirror” filter was added to reject infrared. For nearly a decade, these systems have gathered 1 s exposures at a 3 s cadence whenever solar zenith angle is greater than 102°. They have proven to be extremely reliable, collecting over 350 million images stored in a lossless (gzipped PGM) format.

Many different Starlight-Xpress systems share the same common software interface, so experience with low-cost white-light cameras for THEMIS could be easily extended

GID
3, 753–823, 2013

to color mosaic systems. In this study we focus on two different color cameras provided by Starlight-Xpress: the MX7-C (now "Lodestar-C") using the ICX429AKL CCD with a 4-channel color matrix discussed in Sect. 2.2 and the SXV-H9C with a higher spatial resolution ICX285AQ 3-channel Bayer matrix color CCDs discussed in Sect. 2.1. Of course, there are many other available camera models and manufacturers, but these two provide excellent examples of available color mosaics. They have also been used extensively for applications in auroral science at many locations by several different projects. A summary of locations is given in Table 2, with further details provided below to emphasize the "organic" project evolution facilitated by low-cost devices. Instrument acquisition by groups with different sources of funding may proceed incrementally and deployment plans can be primarily constrained by the availability of existing facilities at remote field sites. The resulting intermittent time-lines for color auroral imaging given below are in striking contrast to the centralized planning and execution involved in a project like THEMIS.

Researchers at the University of Calgary first developed a prototype system combining THEMIS all-sky optics with an MX7C color camera in 2002. The resulting "Rainbow" systems were field tested in Canada during 2003 and at Svalbard for an optical campaign in early 2004 (Partamies et al., 2007). Rainbow system deployment at 8 locations in northern Canada began in 2006 as part of the NORSTAR multi-spectral imaging (MSI) initiative. Sites at Fort Smith (FSMI), Fort Simpson (FSIM), Gillam (GILL), Pinawa (PINA), and Rabbit Lake (RABB) were operated by the Canadian Space Agency (CSA) Canadian Geospace Monitor (CGSM) program; Resolute Bay (RESU) was funded by the US NSF, Saskatoon (SASK) by the University of Saskatchewan, and Yellowknife (YKNF) by CSA. The Canadian network of Rainbow ASIs operates with 5 s exposures at a 6 s cadence in order to maximize sensitivity while facilitating comparison with the 3 s THEMIS cadence as illustrated in Sect. 2.3. More than 35 million high resolution "fast" mode (see Sect. 2.2) images are stored using losslessly compressed PGM files.

Four more Rainbow systems have deployed as part of the Miracle project (Pulkkinen et al., 1998). The first instrument was installed at Nyrölä (NYR) in 2005, followed by two

GID
3, 753–823, 2013

in 1997 at Kevo (KEV) and Muonio (MUO), then another system at Helsinki (HEL) in 2009. From September 2007 the cameras at KEV and MUO were operated in a mode that provided alternating even and odd frames (see Fig. A2b in Appendix A). After 2009 all four systems operated in "fast" mode with images stored in lossy JPEG format.

Another three Rainbow systems have at been operated by Lancaster University at Þykkvibær in south-eastern Iceland (PYKK), at Mánarbakki on the Tjörnes peninsula in north-eastern Iceland (TJRN), and at Húsareyn near Tórshavn in the Faroe Isles (HSRN). The PYKK imager is co-located with the CUTLASS Iceland SuperDARN radar operated by the University if Leicester and shares accommodation and infrastructure with the radar hardware, with the imager mounted in an optical dome installed in the roof of the radar control building. Both the TJRN and HSRN rainbow imagers are installed in enclosures adapted from industrial modular equipment housings. Each weatherproof and thermally-insulated enclosure is mounted on a concrete foundation and is fitted with a bespoke roof that includes a 300 mm diameter optical dome with power and internet routed from nearby buildings. The control computer, power supplies and a dome-heating fan are housed inside the enclosure.

Finally, SRI operates a single Rainbow at Sondrestrom (SND).

The H9C camera was first used in Canada for the Dense Array Imaging System (DAISY, see Partamies et al., 2008). This project consisted of three imagers, each with different optics, all providing fields of view smaller than the typical all-sky configuration. The large number of pixels provided by the ICX285AQ was essential for fully resolving small spatial scales during several campaigns. More recently, a single H9C system has been continuously deployed in Yellowknife (YKNF) as part of the Canadian Space Agency (CSA) AuroraMax project which provides publicly available real-time high-resolution all-sky color auroral images.

The University College London (UCL) Atmospheric Physics Laboratory also operate their own set of color all-sky camera systems for auroral studies; these were developed completely independently of the Rainbow project. Active systems include two H9Cs at Sodankylä (SOD) and Longyearbyen, Svalbard (KHO) and an MX7C at Es-

GID
3, 753–823, 2013

range, Kiruna (KEOPS). These are used primarily as support for the UCL Fabry-Perot Interferometers located all three stations and the Scanning Doppler Imager (SCANDI) at KHO. These instruments measure winds and temperatures by observing Doppler shifts and emission line profiles of the 630 nm and 557.7 nm oxygen emissions. It is essential to have accurate information with regard to cloud cover and auroral structure, so the emphasis has been on qualitative rather than quantitative camera data. For example, contrast stretching is used to enhance auroral features and also the unsharp mask technique used to emphasise auroral structure and increase the visibility of stars. The cameras are operated continuously during the hours of darkness, controlled by an almanac program. Longer exposures than those used for the Rainbow project (typically 20 s) are used, with an interval of 2 min between images. Compared to the images from the previous generation of monochrome all-sky cameras used for this purpose, the improvement in the ability to differentiate between cloud and aurora is dramatic.

2 Color cameras

In this study we examine the spectral response of two very different color mosaic CCDs that have been used for auroral imaging. Some basic parameters of these devices are listed in Table 3. Both detectors use an "interline" architecture in which a single shift moves the contents of each pixel into adjacent masked readout columns. This technique effectively eliminates image smearing during readout and is sometimes referred to as an electronic shutter. Both cameras provide 16 bit data, although effective dynamic range is slightly reduced by a device dependent constant DC offset that is usually on the order of 1000 data numbers.

Both types of cameras have recently been calibrated in a darkroom facility at the University of Calgary. The primary light source was an incandescent tungsten filament lamp driven by a constant current source. Lamp light was passed through an Acton Research model SP-500i single grating monochromator with a 1200 line mm^{-1} grating and 50 micron slit spacings with a 0.65 nm wavelength resolution. A Newport model

GID
3, 753–823, 2013

918D-SL-OD1 photodiode with absolute spectral response traceable to NIST standards was used to correct for intensity variations in wavelength due to the source blackbody and monochromator grating characteristics.

Two pinholes of approximately 3 mm diameter separated by about 60 cm were used to create a collimated beam. This was directly incident on the CCD (with the lens removed from the camera). Image exposures of 400 ms were acquired for wavelengths ranging from 300 nm to 1000 nm at 1 nm intervals. Some variation in actual exposure time was expected due to the use of a non "hard" real-time operating system; actual jitter was typically less than 1 ms with rare exceptions on the order of ±10 ms (~ 2 %). Immediately following the CCD measurements, the Newport photodiode was inserted in front of the camera and the wavelength scan was repeated.

An example portion of a single calibration frame is shown in Fig. 2. A very small-scale grid pattern is produced by the Bayer matrix response to monochromatic light. The coarse grid is a moiré artifact that depends on the figure display size and resolution. Isolated circular patterns correspond to dust on the CCD window.

Background ("dark") levels were estimated from image corners. The observed count statistics were consistent with a shifted Gaussian, which was modelled with a constant bias term added to a Poisson distribution. Results for each device were constant over multiple calibration scans. The ICX285AQ CCD used for this study had a DC bias of roughly 3560 counts and a Poisson mean of 30 counts for a 400 ms exposure. The ICX429AKL unit had a bias of roughly 1565 counts and a Poisson mean of 25 counts in 400 ms. Our experience with other similar systems is that each device has a unique invariant bias, usually in the range of 1000–4000 data numbers.

Pixels were grouped according to color channel by indexing on a 2×2 sub grid (see Figs. 4 and 6). Any saturated values were excluded from subsequent analysis. Total counts were summed in each channel, background corrected, and normalized using the calibration photodiode measurement. Figure 3 shows an example of the unnormalized spectral response for each color channel of the Sony ICX285AQ CCD (see next section) along with the corresponding reference diode power level.

GID
3, 753–823, 2013

Very similar calibration configurations were used for all of the results presented here, but there is no guarantee of absolute consistency. This means that, in contrast to Sigernes et al. (2008, 2009), our results cannot be used for absolute sensitivity (i.e. counts/Rayleigh) comparisons between different cameras. They do, however, provide simultaneous self-consistent results for all color channels on each CCD.

2.1 Sony ICX285HQ

The SXV-H9C camera uses a Sony ICX285AQ CCD with 3-color Red/Green/Blue (RGB) microfilters arranged in a standard Bayer matrix pattern (shown in Fig. 4). Three color values at each pixel location can be easily determined by interpolation from neighboring pixels (e.g. Gunturk et al., 2005), with Bayer de-mosaicing support built into many image processing software packages. The density of green pixels is twice that of red and blue; this configuration can be advantageous for observing aurora which are often dominated in visible wavelengths by 557.7 nm atomic oxygen "green-line" emissions. Filter passbands (Fig. 4) are similar to the three different types of color sensitive cones in the human eye. One notable difference is the significant sensitivity in the near infra-red (NIR) with essentially identical response in all three channels for wavelengths greater than 800 nm. The standard read-out mode uses a progressive scan, so a single frame can contain all active pixels.

2.2 Sony ICX429AKL

The MX7C camera has a Sony ICX429AKL CCD with 4-color Cyan/Yellow/Green/Magenta (CYGM) channels. The microfilter mosaic layout on the CCD is shown in Fig. 5, but typical operating modes produce a slightly different result. Complications arise from the fact that the ICX429AKL readout mode is interlaced (Appendix A), so that all pixels cannot be read out simultaneously. Figure 6a shows the native ("raw") color mosaic along with the output for frames containing only even

GID
3, 753–823, 2013

and odd lines (Fig. 6c and d). Response curves in Fig. 5 were produced by combining results from even and odd frames.

Separate exposures and readout mean that the even and odd frames will not correspond to exactly the same time interval. Differences on the order of a few seconds may be unimportant for a stable laboratory calibration, but can be a real concern under field conditions when observing highly dynamic aurora.

Fortunately, the MX7C camera software does support a "fast" readout mode which sums over adjacent rows (i.e. $1+2$, $3+4$, ...) and returns the result as a single half-height frame with an effective color mosaic as shown in Fig. 6b. Data acquired in this "fast" mode was used to produce the response curves shown in Fig. 7.

2.2.1 Linear independence

ICX429AKL "fast" mode data are produced by binning adjacent rows of "raw" pixels. This transformation can be expressed as a matrix multiplication which converts from raw (i.e. cyan and green) to binned (i.e. cyan + green) color channels.

$$\begin{bmatrix} 0&1&1&0 \\ 1&0&0&1 \\ 0&1&0&1 \\ 1&0&1&0 \end{bmatrix} \begin{bmatrix} \mathrm{Cy} \\ \mathrm{Ye} \\ \mathrm{Gr} \\ \mathrm{Mg} \end{bmatrix} = \begin{bmatrix} \mathrm{Gr}+\mathrm{Ye} \\ \mathrm{Mg}+\mathrm{Cy} \\ \mathrm{Mg}+\mathrm{Ye} \\ \mathrm{Gr}+\mathrm{Cy} \end{bmatrix} \quad (1)$$

This equation naturally suggests the possibility of reversing the process in order to obtain the four underlying raw channels from four fast channels. Unfortunately, the 4×4 transformation matrix is singular (zero determinant) and cannot be inverted, meaning that the row binning process is irreversible. One goal of this paper is to better understand how this loss of information impacts spectral resolution.

GID
3, 753–823, 2013

2.3 THEMIS/Rainbow sensitivity comparison

The THEMIS all-sky imager network uses Starlight Xpress model MX7 (now "Lodestar") cameras with Sony ICX429AL CCD detectors. These are monochrome devices that are identical to the ICX429AKL CCD, except without the microfilter mosaic. Consequently, every pixel in the ICX429AL has an identical very broad ("white light") spectral response. This is ideal for maximizing the photon count rate under low-light conditions, but data can not be used to distinguish between different emission wavelengths. Like the MX7C, the MX7 is also an interline system with driver software that can either read alternate rows or the sum of row pairs ("fast" mode). The THEMIS optics project an all-sky image onto a 512 × 512 pixel sub-region of the CCD that is read in fast mode with column pairs subsequently binned to produce a 256 × 256 array of approximately square super-pixels. Images are acquired at a 3 s cadence with 1 s exposures; this 33 % duty cycle reflects a combination of constraints in the camera, serial communications (USB 1.1), and a relatively low-power system computer.

The MX7C based "Rainbow" systems currently operated by the Calgary and Lancaster groups use all-sky optics that are essentially identical to those in the THEMIS system, and both systems use CCDs with identical dimensions and pixel density. Rainbow systems operate at a slower 6 s cadence with longer 5 s exposures designed to compensate for anticipated losses due to the color mosaic micro-filters. Stored image frames consist of 512 × 256 rectangular superpixels with 4 "fast" color channels as described previously. During post-processing these multi-channel images can be binned by column pairs to produce 256 × 256 superpixels with the same geometry as THEMIS. Each superpixel is composed of 4 device level ("raw") pixels with the same channel combination in every case: Cy + Gr + Ye + Mg. The result is a monochrome image with a very wide spectral response that is an average of the four mosaic color passbands.

A monochrome Rainbow image is convenient for certain kinds of analysis that do not require spectral information (e.g. star tracking). It can also be used for a comparison of

GID
3, 753–823, 2013

the relative sensitivity of the two systems. For several years (2009–2013) a Rainbow system has been operating near Fort Smith in northern Canada at a field site that is only a few kilometres from a THEMIS system. Both cameras are looking towards local zenith, but are oriented along slightly different azimuths. A pixel-by-pixel comparison would require precise determination of both camera orientations followed by careful mapping into a common coordinate system.

For this study we shall consider only frame average count rates, which are a robust measure of whole system response that are not sensitive to orientation errors or minor inhomogeneities in CCD response. Count rates from the two different cameras are usually very highly correlated, as illustrated by an hour of auroral data shown in Fig. 8. The relatively high (87 %) Rainbow to THEMIS count rate ratio is presumably due to 3 of 4 color channels having transmission maxima near the brightest auroral green-line (557.7 nm) emissions. Although the Rainbow systems do have a lower cadence than THEMIS (6 vs. 3 s) they have a much higher (250 %) effective duty cycle (5 vs. 1 s exposures). As currently operated, a Rainbow camera can produce white-light images with more than twice the number of counts from THEMIS over the same interval. This could improve the ability to detect faint structures, albeit at the cost of temporal resolution.

Color imagers can also provide information about auroral spectra that is not accessible to white-light cameras. For example, Rainbow to THEMIS count rate ratios varied by approximately 10 % over the interval shown in Fig. 8 with the higher ratios tending to correspond to higher count rates. This is consistent with an increase in characteristic precipitation energy causing a change in the relative intensity of different auroral emissions. A quantitative analysis is beyond the scope of this paper, and will be the focus of a subsequent study.

2.4 Infra-red rejection

Dark-room results were obtained using the simplest possible configuration: light from a calibration source directly incident on the thermal glass window in front of each CCD. For field operations there are usually several additional optical elements. Most of these

GID
3, 753–823, 2013

are part of the "fish-eye" lens system required to image a hemispherical ("all-sky") field of view and project it onto the CCD. While there can be significant losses due to reflections between multiple glass surfaces, the overall transmission for these components should be nearly uniform across the visible spectrum.

The THEMIS and Rainbow systems also have an additional filter (Fig. 9) to reject near infra-red (NIR) photons above 750 nm. This "hot mirror" was included to reduce the effects of chromatic aberration over a wide range of wavelengths. Limiting the input light to visible wavelengths was intended to reduce undesirable image blurring. One drawback of this particular filter is the substantial (50 %) attenuation at shorter wavelengths, which is unfortunate considering the importance of blue (e.g. 391.4 and 427.8 nm) auroral emissions. It could also be argued that NIR auroral features are a sufficiently important source of information to outweigh the deficits of slightly less well focused images. One of the original motivations for this study was a comparison of THEMIS spectral response with and without the hot mirror, and the possibility of differencing data from two different cameras to estimate the NIR contribution.

Given that NIR blocking filters have been used in many of the systems considered in this study, we will include their effect in most of the analysis that follows. This is done using modified CCD response functions produced by multiplying calibrated sensitivity for each device (shown in Figs. 4, 5, and 7) by the hot mirror transmission curve in Fig. 9. We did also repeat the analysis without NIR blocking and found some interesting differences that are explored further in Sect. 3.3.

3 Spectral estimation

An ideal color camera would generate images that are perceived by the human eye to be indistinguishable from the source. Practically speaking, this usually means acquiring a rectangular array of $N_x \times N_y$ pixels, each of which has a red/green/blue (RGB) triplet of color intensities. When properly displayed, viewing the image frame should produce the same retinal response as when observing the original scene. The field of color

GID
3, 753–823, 2013

studies is quite complex and requires an understanding of topics including basic optics, biology, and human perception. In this study we deliberately chose to work only with very simple models of color. Our primary focus is the exploration of possibilities for dealing with color CCDs as multi-spectral detectors.

To start, consider an ideal linear detector with three different channels. The channel spectral passbands are chosen to exactly match the wavelength sensitivity of the three different types of cones $c_k = [c_1, c_2, c_3] \approx$ [R,G,B] in the human eye. Measurements from this detector $m_k = [m_1, m_2, m_3]$ should be identical to the cone response. The Bayer matrix CCD in Sect. 2.1 is a good approximation to this ideal detector, with three measurement channels that correspond to the primary colors

$$[m_1, m_2, m_3] \approx [c_1, c_2, c_3] \tag{2}$$

Differences between real and ideal detectors can be modelled by some kind of transformation to convert from measurements to true-color. In general, there can be more than three measurement channels, and a different functional form may be needed for each color

$$c_i = f_i(m_1, m_2, \ldots, m_j) \tag{3}$$

Many transformations can be usefully expressed as linear combinations of measurements m_j from N_m measurement channels; multiplying by weighting coefficients d_{ij} to get N_c color channel estimates c_i

$$c_i = \sum_j d_{ij}\, m_j \tag{4}$$

which can be written more compactly as a matrix multiplication

$$\mathbf{c} = \mathbf{D}\,\mathbf{m} \tag{5}$$

For an ideal 3-channel Bayer RGB mosaic the weights **D** might be a 3×3 identity matrix, with a CYGM mosaic requiring a more complicated 3 × 4 matrix.

GID
3, 753–823, 2013

In auroral physics, color is really only important as a measure of spectral features corresponding to interesting atomic and molecular emissions. From this perspective, a more useful activity would be to somehow combine multi-channel observations in order to estimate spectral intensity $\tilde{s}(\lambda)$ at specific wavelengths of interest, i.e.

$$\tilde{s}(\lambda) = \sum_n d_n(\lambda)\, m_n \tag{6}$$

We can not reasonably expect to recover high-resolution spectra from a small number of wide-band observations. It is, however, useful to explore the merits of this approach to dealing with color mosaic CCD data.

In general, a spectrum $s(\lambda)$ is observed using a linear device with N_m different measurement channels. Each channel may have a different spectral response given by "kernel" $K_i(\lambda) = K(\lambda_i, \lambda)$, where λ_i is some characteristic (i.e. peak or average) wavelength corresponding to each channel. The result will be N_m measurements $\tilde{m}(\lambda_i)$, each with some noise contribution $n(\lambda_i)$.

$$\tilde{m}(\lambda_i) = \int K(\lambda_i, \lambda') s(\lambda') \mathrm{d}\lambda' + n(\lambda_i) \tag{7}$$

In an ideal instrument the measurement kernels should be extremely narrow (i.e. Dirac delta functions) and the noise negligible ($n \approx 0$), so the observations would be an accurate measure of the original source spectrum.

$$\tilde{m}(\lambda_i) = \int \delta(\lambda_i - \lambda') s(\lambda') \mathrm{d}\lambda' + n(\lambda_i) \;\approx\; s(\lambda_i) \tag{8}$$

For wide-band color CCDs the kernels are definitely not delta functions and Poisson noise is unavoidable.

Fortunately, this general class of problems arises in many different applications and has been addressed in detail by numerous authors (e.g. Rodgers, 1976, 1990; Menke, 1989; Aster et al., 2005; Tarantola, 2005). Methods for solving these problems are

GID
3, 753–823, 2013

variously referred to as linear inversion or retrieval or estimation; the shared goal is to infer useful results from a limited number of non-ideal observations in the presence of noise.

One effective procedure is to first discretize the integral in Eq. (7) and replace it with a finite sum

$$\tilde{m}(\lambda_i) \approx \sum_j q_j \, K(\lambda_i, \lambda_j) \, s(\lambda_j) \Delta\lambda + n(\lambda_i) \tag{9}$$

where q_j are quadrature weights (i.e. trapezoidal rule, Simpson's rule). This leads to a matrix representation

$$\tilde{\mathbf{m}} = \mathbf{K}\mathbf{s} + \mathbf{n} \tag{10}$$

which is not solvable in general because $\mathbf{K}$ may not be a square matrix and thus cannot be directly inverted. A solution can, in principle, be obtained by applying the pseudo-inverse

$$\left[\mathbf{K}^{\mathrm{T}}\mathbf{K}\right]^{-1} \mathbf{K}^{\mathrm{T}}\tilde{\mathbf{m}} = \mathbf{D}\tilde{\mathbf{m}} \tag{11}$$

$$= \mathbf{D}\mathbf{K}\mathbf{s} + \mathbf{D}\mathbf{n}$$

$$= \mathbf{A}\mathbf{s} + \mathbf{e} = \tilde{\mathbf{s}} \tag{12}$$

where rows of the matrix $\mathbf{D}$ in Eq. (11) are called "contribution functions" (also referred to as inverse response kernels) that indicate what combination of observations should be used to estimate the spectrum at a given wavelength.

Rearranging terms shows that the recovered spectral estimate $\tilde{\mathbf{s}}$ consists of two parts (Eq. 12). The first term is a synthetic measurement of the true spectrum as viewed through a set of "averaging" or "windowing" functions $A(\lambda_i, \lambda)$ constructed from a combination of the contribution functions and the measurement kernels. Ideally, the averaging functions A would be extremely narrow and $\mathbf{A}$ would be an identity matrix.

GID
3, 753–823, 2013

In practice each averaging function $A_i(\lambda)$ will have some finite width corresponding to the effective resolution limit. A very broad averaging function means that the retrieval process can only recover a highly smoothed version of the underlying spectrum.

The second part of Eq. (12) is an error term arising from a combination of contribution functions and measurement noise. In practice the actual noise values n_i are unknown, so we must use estimates $\tilde{n}_i$ (e.g. $\tilde{n} = \sqrt{m}$ for Poisson noise) to estimate the retrieval error

$$\tilde{e}_i = \sqrt{\sum_j D_{ij}^2 \tilde{n}_j^2} \tag{13}$$

which obviously should be made as small as possible. Unfortunately, resolution and error are inextricably connected, and it is usually necessary to accept some trade-off with sub-optimal resolution in return for moderate levels of error.

One popular class (Menke, 1989; Aster et al., 2005) of linear retrieval techniques, called Tikhonov regularization, applies smoothness constraints to the recovered profile $\tilde{s}(\lambda)$ in order to damp spurious oscillations driven by measurement noise. An alternative formalism (Backus and Gilbert, 1968, 1970; Parker, 1972) attempts to simultaneously minimize the retrieved variance along with the "spread" (q_2) of the resolution functions

$$q_2(\lambda) = 12 \int (\lambda - \lambda')^2 A(\lambda, \lambda')^2 \, \mathrm{d}\lambda' \tag{14}$$

to obtain contribution functions given by

$$\mathbf{d}(\lambda) = \frac{\boldsymbol{k}^{\mathrm{T}} [\mathbf{Q}(\lambda) + \mu \mathbf{C}]^{-1}}{\boldsymbol{k}^{\mathrm{T}} [\mathbf{Q}(\lambda) + \mu \mathbf{C}]^{-1} \boldsymbol{k}} \tag{15}$$

where $\boldsymbol{k}$ is a column vector of the kernel areas ($k_i = \int K_i(\lambda) \mathrm{d}\lambda$), $\mathbf{C}$ is the measurement covariance matrix, $\mathbf{Q}(\lambda)$ is the spread matrix

$$Q_{ij}(\lambda) = 12 \int (\lambda - \lambda')^2 K_i(\lambda') K_j(\lambda') \, \mathrm{d}\lambda' \tag{16}$$

GID
3, 753–823, 2013

and μ is a Lagrange multiplier that can be used to select trade-offs between the extremes of high resolution ($\mu = 0$) and low noise ($\mu = \infty$).

The Backus–Gilbert approach is more computationally intensive than many other regularization techniques, but provides a clear picture of how error and resolution respond to a single control parameter. It is particularly useful for exploring the effective resolution of a hypothetical set of measurements, and how changing measurement details might improve the amount of retrieved information.

3.1 ICX285AQ (H9C)

Backus–Gilbert analysis was carried out using the three ICX285AQ response curves from Fig. 4 as measurement kernels. Resolution and contribution functions were calculated for a wide range of visible wavelengths with a fixed smoothing parameter ($\mu = 1$). The contribution functions (D) are presented in Fig. 10, and clearly reflect the three RGB channels of the filter mosaic. For example, estimating the "true" spectral intensity at 550 nm is accomplished using primarily the green channel, with minimal contributions from the other two. At wavelengths away from the filter transmission peaks, retrieval involves a mixture of two or more channels. For example, the best estimate for spectral intensity at 510 nm is obtained by combining roughly equal amounts of the blue and green channels. This would appear to suggest that useful spectral estimates can be determined for any arbitrary wavelength.

Practical limitations become apparent after examining the resolution (A) functions. Figure 11 shows resolution functions calculated for several different auroral emissions given in Table 1. There should ideally be seven distinct resolution functions, one centered on every desired wavelength, and each only a few nanometres in width. This would allow us to make independent estimates of the luminosity at each wavelength without any contamination from nearby emissions.

The actual outcome is only three sets of resolution functions with widths of 50–100 nm. All of the blue wavelengths produce nearly identical resolution functions, meaning that it is impossible to distinguish between the four most commonly consid-

GID
3, 753–823, 2013

ered auroral emissions. More usefully, the green wavelength has a resolution function that is only minimally sensitive to the brightest blue and red emissions. Like the blue emissions, results for different red-line and NIR emissions are effectively indistinguishable.

For wavelengths near the center of each channel the effective resolution is very similar to the corresponding filter transmission curve. However, attempted retrieval at intermediate wavelengths is completely ineffective, producing resolution functions that are essentially the same as one of the primary colors. The underlying measurements simply do not contain enough information to produce different resolution functions away from the three channel centers.

The overall pattern of how resolution functions change with retrieval wavelength can be represented as a two-dimensional grid, where each column is the resolution function at a particular wavelength. Figure 12a contains a contour plot of this resolution surface for the H9C camera. This clearly shows that there are three distinct sets of resolution functions, all with full-width half-maximum (FWHM) on the order of 100 nm, centered near 480 nm, 530 nm and 620 nm respectively.

These results indicate that the H9C can only usefully distinguish between three independent spectral ranges, each strongly resembling one of the measurement kernels. More precise wavelength discrimination, such as trying to separate N_2^+ (470.9 nm) and H_β (486.1 nm) emissions, is simply not possible given the measurement characteristics of this device.

3.2 ICX429AKL (MX7C)

Backus–Gilbert analysis applied to the ICX429AKL "fast" mode measurement kernels in Fig. 7 produces resolution functions as shown in Fig. 13. These results are similar to those from the H9C, with only three distinct resolvable channels. The blue channel is slightly narrower, green is slightly wider, red is very similar, and the resolution contours in Fig. 12b are essentially the same.

GID
3, 753–823, 2013

Analysis of the "raw" mode kernels from Fig. 5 produces resolution functions as shown in Fig. 14. While there are still only three distinct resolution functions, the blue channel is significantly narrower than for the "fast" mode. Resolution contours in Fig. 12c are also substantially improved. Access to data from all four native color channels on the ICX429AKL is clearly beneficial, albeit only incrementally better than "fast" mode or 3-channel ICX285AQ observations.

As mentioned previously, Backus–Gilbert analysis involves a tunable parameter μ which controls the trade-off between resolution and error. For cases with many different measurement kernels this can be used to make significant changes in the retrieval results. For the case of a 3- or 4-channel color camera the μ parameter has very little effect, as it is simply not possible to construct very different combinations of kernels. A typical example is given in Fig. 15 showing spread vs. noise for a wide range of μ. The trade-off curve has the characteristic shape, but both spread and noise vary only over an extremely small range. This is true even for much smaller or larger values of μ. Consequently, in this study we restrict our analysis to a nominal value of $\mu = 1$.

3.3 Infra-red rejection

As mentioned in Sect. 2.4, many auroral imagers are operated with a "hot mirror" to reject infra-red wavelengths. Consequently, most analysis in this study has been carried out assuming the presence of such a filter.

For completeness we have also studied the effects of including the entire 300–1000 nm wavelength range covered by our calibration. These results are shown in Fig. 16 and exhibit significant differences from those obtained using only the visible spectrum. The reason for this is that Backus–Gilbert analysis attempts to minimize window function amplitude by combining different measurement kernels. However, as shown previously, all CCD channels have very similar response curves above 750 nm. The result for a H9C system are clearly sub-optimal, with all cases containing significant NIR contributions. MX7C fast mode results are similarly degraded. Interestingly,

GID
3, 753–823, 2013

the MX7C raw mode produces essentially the same blue, green, and red channels as before, but with additional distinct NIR channel.

3.4 RGB estimation

The central theme of this study is the examination of color mosaic CCDs in terms of their capabilities for spatial resolved multi-spectral analysis of the aurora. It is admittedly also important to be able to produce colorful images for scientific communication and public outreach. As noted previously, color science is a complicated topic that combines physics, biology, and psychology. For this study we take a very simple approach: using Backus–Gilbert methods to retrieve wavelengths corresponding to each of the three primary colors. In other words, we determine a contribution matrix **D** as in Eq. (5) that will produce a color triplet **c** from an arbitrary set of measured channel intensities **m**. The primary colors are selected to match CIE 1931 (Wyszecki and Stiles, 2000).

$$\mathbf{c} = \begin{bmatrix} 700.0\,\mathrm{nm} \\ 546.1\,\mathrm{nm} \\ 435.8\,\mathrm{nm} \end{bmatrix} \tag{17}$$

For a ICX285AQ CCD the RGB contribution matrix has the relatively simple form given in Eq. (18). The matrix is approximately diagonal, so each primary color is dominated by a single channel, with a scale difference that reflects higher sensitivity to red wavelengths and lower sensitivity to blue.

$$\mathbf{c} = \begin{bmatrix} +0.27631 & +0.01982 & +0.04673 \\ -0.07100 & +0.65894 & -0.04815 \\ -0.00980 & +0.02675 & +1.00000 \end{bmatrix} \begin{bmatrix} \mathrm{R} \\ \mathrm{G} \\ \mathrm{B} \end{bmatrix} \tag{18}$$

The RGB contribution matrix for the MX7C fast mode is given in Eq. (19). There is a similar scale difference reflecting greater CCD sensitivity to red wavelengths, but the matrix is not nearly diagonal due to the more complex relationship between device

GID
3, 753–823, 2013

channels and the primary colors.

$$\begin{bmatrix} -0.03366 & +0.06239 & +0.14099 & -0.09326 \\ +0.13351 & -0.30245 & +0.04012 & +0.37995 \\ -1.00000 & +0.07095 & +0.41522 & +0.81462 \end{bmatrix} \begin{bmatrix} \mathrm{Gr}+\mathrm{Ye} \\ \mathrm{Mg}+\mathrm{Cy} \\ \mathrm{Mg}+\mathrm{Ye} \\ \mathrm{Gr}+\mathrm{Cy} \end{bmatrix} \quad (19)$$

The RGB contribution matrix for the MX7C raw mode is given in Eq. (20). There is a similar scale difference reflecting greater CCD sensitivity to red wavelengths and a complex mapping from device channels to primary colors.

$$\begin{bmatrix} -0.14878 & -0.06312 & +0.16537 & +0.15974 \\ +0.30838 & +0.25822 & -0.26835 & -0.25324 \\ +1.00000 & -0.02615 & -0.97716 & +0.02779 \end{bmatrix} \begin{bmatrix} \mathrm{Cy} \\ \mathrm{Ye} \\ \mathrm{Gr} \\ \mathrm{Mg} \end{bmatrix} \quad (20)$$

Figure 17 contains a summary of the RGB conversion matrices applied to the calibration scans. The top color bar was produced using a direct mapping from Bayer pixels to RGB (i.e. **D** is the identity matrix); the other three were calculated using Eqs. (18)–(20).

3.4.1 Estimation error

The estimation error ϵ due to measurement noise n can be calculated for any specific situation using Eq. (13). Assuming roughly equal noise n in each measurement channel leads to a useful approximation

$$\epsilon = \sqrt{\Sigma d_i^2 \, n_i^2} \approx n\sqrt{\Sigma d_i^2} \qquad n_i \sim n \quad (21)$$

that indicates how sensitive an estimated value is to the presence of measurement noise. As shown in Table 4, the three different cases (corresponding to Eqs. 18–20) are all roughly the same for each color channel.

GID
3, 753–823, 2013

3.5 Combinations and modifications

It would be very useful to have a single camera with more than 3 or 4 spectral channels, such as might be produced by a large CCD with a 3×3 mosaic of 9 different color channels. Until such a device becomes available it will be necessary to explore alternatives which are based on combinations and modifications of existing technology.

An obvious first step would be to combine the two different CCDs considered in this study. While both are effectively 3-channel devices, there are enough differences between the filter response profiles to suggest that such a combination would be worthwhile. This turns out to be the case, as can be seen from results of a H9C/MX7C (fast mode) Backus–Gilbert analysis shown in Fig. 18a. Using 7 different filters provides at least four distinct spectral bands, with resolution on the order of 50 nm.

Further improvements could presumably be achieved with the addition of some different color channels. However, virtually all available commercial CCDs use either RGB or CYGM color mosaics. One exception is the Sony ICX456 with a RGBE (merald) mosaic, but the standard output appears to have only 3 RGB channels. Even if direct access to the sensor were possible, it would only provide a single additional channel, and thus only marginally enhance spectral resolution.

There are also very significant challenges associated with merging images from two or more different types of cameras. It may be difficult to synchronize exposure and readout times. Precise calibration is required to correct for different sensitivities. Pixel size and density differences will complicate the process of spectral retrieval at common locations.

It would be easier to combine data from two or more identical cameras, although for effective spectral retrieval it would of course be necessary to have different passbands for each system. An ideal configuration might be to simply shift one set of filter responses by some $\Delta\lambda$ chosen to maximize effective resolution. However, this is not an option for wide-band color mosaic filters, unlike narrow-band interference filters which can be tilted to produce minor shifts to longer wavelengths.

GID
3, 753–823, 2013

The combination of a broad-band CCD and a narrow-band transmission filter (Fig. 19a) is commonly used in auroral studies to isolate specific emission lines. These measurements can be further improved by taking additional measurements at nearby wavelengths to estimate and remove "background" light levels. Equivalently, spectral intensity at a single wavelength could be determined by taking the difference between unfiltered broad-band signal levels and those obtained using a narrow-band rejection ("notch") filter (Fig. 19b).

Measuring brightness at several different wavelengths with a single wide-band CCD (Fig. 19c) will require the use of multiple filters or a single tunable filter (López-Alvarez et al., 2008; Sigernes et al., 2012; Goenka et al., 2013). In either case, the measurement process will involve a sequence of observations that are intrinsically non-simultaneous. This may be a significant problem for sources, such as the aurora, that are often highly dynamic over short time scales. The obvious solution would be to simultaneously operate two or more systems with identical CCDs and different filters. Successful examples of this approach include the all-sky Polar Camera ("PoCa" Steele and Cogger, 1996) using two cameras each with a 5 channel filter wheel and the Auroral Structure and Kinetics narrow field imager ("ASK" Dahlgren et al., 2008) using three cameras each with a single filter. However, truly simultaneous operation of multiple CCDs is complicated, produces large amounts of data, and becomes increasingly difficult for a large number of different wavelengths.

A perhaps less obvious approach takes advantage of the fact that a single complex filter can have a different effect on each channel of a color camera. For example, consider a single RGB CCD system which has an single filter with three narrow pass-bands at 427.8 nm, 557.7 nm, and 630.0 nm (Fig. 19d). This device can provide truly simultaneous images at three different wavelengths, albeit with lower sensitivity and spatial resolution than a single channel system.

Next, consider two identical RGB CCDs, one with a single multi-notch filter that rejects three different narrow pass-bands. One system measures signal plus background in three wide-band channels, while the other system will effectively measure three wide-

GID
3, 753–823, 2013

band background channels with minimal signal contributions. The difference between images from these two systems will thus contain three channel differences, each of which can be used to infer the background corrected signal intensity at a different notch wavelength.

One related design strategy might be to select transmission or rejection wavelengths appropriate for a given camera response and auroral features of interest. This would require custom multi-feature narrow-band filters, which can be relatively expensive compared to the cost of a single color camera. For this study we start by considering a stock multi-notch filter (Semrock NF01-405/488/561/635) with a spectral transmission profile as shown in Fig. 20. A hypothetical two camera (both MX7C fast mode) system with one multi-notch filter was subjected to Backus–Gilbert analysis, with results as shown in Fig. 18b. As expected, very good spectral resolution (< 40 nm) can be obtained at three notch wavelengths, and moderate resolution (> 50 nm) in several other ranges. For comparison, a similar analysis was carried out using a hypothetical combination of two MX7C cameras and a different filter with multiple passbands (Semrock FF01-440/521/607/694). Results shown in Fig. 18c indicate a similar enhancement in resolution, albeit at a different set of wavelengths.

We have explored several other options for dual camera systems. One of the more successful configurations did not require abrupt notches or passbands, but instead used a gradually modulated sinusoidal transmission profile (Fig. 19e) given in Eq. (22).

$$\frac{1}{4}\sin\left(\frac{\lambda}{\lambda_0}+\phi_0\right)+\frac{3}{4} \qquad \lambda_0 = 17.0\,\text{nm},\ \phi_0 = 0 \tag{22}$$

While this particular filter was not selected from a catalog, we do expect that a custom order might not be prohibitively expensive, especially given that the specific details do not drastically alter the outcome. Results shown in Fig. 18d clearly indicate that this simple combination is even better than a more complicated H9C/MX7C pair, providing good resolution over a wide range of visible wavelengths.

The obvious next step is to consider combinations of three cameras. Two MX7C fast mode systems using different notch filters and a third unmodified device produce res-

GID
3, 753–823, 2013

olution functions as shown in Fig. 21a. This configuration is only slightly better than either notch filter separately, although it is possible that a custom configuration could be significantly better. For comparison we analyzed a 3 camera system with simple wavelength shifts of $\Delta\lambda = \pm 9$ nm and obtained results shown in Fig. 21b. This purely hypothetical combination provides excellent resolution over a wide range of visible wavelengths. Very good results (Fig. 21c) were also produced by a physically achievable combination of two sinusoids with different periods and phase offsets ($\lambda_1 = 17.0$ nm, $\phi_1 = -\pi/4$, $\lambda_2 = 21.0$ nm, $\phi_2 = +\pi/4$). This provides spectral estimation with 50 nm or better resolution over most of the visible spectrum.

3.5.1 Quantitative comparison

Contour plots of the window functions, such as those shown in Fig. 21, provide a useful picture of the spectral resolution for a hypothetical system of filters and detectors. However, they are less well suited for quantitative comparison of two or more different systems. For that, we consider certain key Backus–Gilbert parameters as a function of wavelength. Two useful parameters have already been introduced: spectral resolution given by the "spread" (q_2 defined in Eq. 14) and sensitivity to measurement error given by the "noise" parameter (Eq. 13). We also introduce a third useful quantity: "bias" (q_3) to measure whether window functions are offset from the retrieval wavelength.

$$q_3(\lambda) = \int (\lambda - \lambda') A(\lambda, \lambda') \, \mathrm{d}\lambda' \tag{23}$$

Figure 22 shows how these three parameters vary as a function of wavelength for several of the cases considered previously. Spectral resolution is generally poor outside the range of visible wavelengths due to low CCD sensitivity below 400 nm and hot mirror NIR rejection above 750 nm. All cases achieve similar resolution quality around 650 nm, but only the H9C/MX7C and 3 × MX7C double-modulated configurations provide equally good results for all wavelengths above 400 nm. Noise levels are comparable for most cases, but are roughly twice as large for the modulated configurations.

GID
3, 753–823, 2013

The 3×MX7C double-modulated configuration provides minimal bias from 450–750 nm, H9C/MX7C in a narrower range, and all other cases exhibit considerable bias except around 650 nm.

Initial values for the modulation parameters in Eq. (22) were determined manually. This process was tedious and did not guarantee an optimal outcome. In order to automate the search through parameter space several different metrics were tested, with the best results being obtained for the average bias $\overline{q}_3$

$$\overline{q}_3 = \frac{\int q_3(\lambda)\,\mathrm{d}\lambda}{\int \mathrm{d}\lambda} \tag{24}$$

integrated over the wavelength range 450–650 nm. Final values for the single and double modulated configurations were obtained by automated minimization of $\overline{q}_3$ starting from several different initial conditions.

4 Discussion

In this study we have examined several aspects of color mosaic CCD with applications for auroral imaging. The Backus–Gilbert formalism proved to be very convenient for comparing spectral resolution of existing devices. It also provided a quantitative basis for future instrument design and optimization. Finally, it can be used as an alternative method for RGB channel estimation.

Our original goal was to obtain a quantitative comparison of the spectral response for a Sony ICC429AKL CCD for native ("raw") and standard ("fast") read-out modes. Results in Fig. 12b, c clearly show that data from both modes can effectively distinguish between only three different wavelength ranges. The raw mode does provide slightly better resolution for blue and green wavelengths, as can also be seen by comparing Figs. 13 and 14. It is also better able to resolve different color bands in the absence of a NIR blocking filter, as shown in Fig. 16. Based only on these considerations, the logical choice would be to acquire data in raw mode whenever possible.

GID
3, 753–823, 2013

As a practical counter argument, the existing MC7C camera configuration does not appear to support direct readout of the full CCD. An fairly good approximation ("pseudo-progressive", see Appendix A) may be possible, but provides color channels that are not exactly simultaneous. The importance of this effect will depend on the ratio of exposure to read-out time, and could be an issue for rapid auroral variations. A pseudo-raw image frame data stream would also be double the size of fast mode frames, requiring increased operational and financial resources (e.g. storage, telemetry, processing). Still, exploring the feasibility of alternate read-out modes does seem to be worthwhile.

Results shown in Fig. 12a and b indicate that the H9C spectral resolution is comparable to the MX7C fast-mode. Although the ICX285AQ and ICX429AKL CCDs use very different color filter passbands, Backus–Gilbert analysis shows that both devices will produce essentially the same information. This result is not surprising, as both CCDs were presumably designed to achieve the same goal: distinguishing between three primary colors.

While the effective spectral response of the two CCDs are very similar, they are not identical. This means that combining data from two different cameras could theoretically provide better wavelength resolution than either device separately. Analysis shows that an ideal MX7C/H9C combination (Fig. 18a) would be able to distinguish between at least 4 different spectral bands. This significant spectral improvement over a single 3 channel system would also be accompanied by an increase in total count rate due to the effective doubling of optical and detector area.

In practice, combining data from two different types of cameras is not a simple process. Even starting with identical front-end all-sky lenses, different transfer optics would be required to match the image field-of-view to CCDs of different size. Further differences in pixel size, density, and color mosaic pattern must also be accounted for in order to merge results. Finally, the two cameras must either be identically oriented (which can be difficult to ensure over long durations at remote field sites) or images must be carefully corrected for alignment differences. These issues are not insurmountable, but

GID
3, 753–823, 2013

it is not obvious whether the necessary effort is justified by the enhanced spectral resolution.

Merging data is simpler for cameras with identical CCDs and optics, although this will only produce enhanced spectral resolution if the devices have different response functions. This can be achieved with simple color filters, as shown by Valero et al. (2007) who used sequential observations through different acrylic filters (e.g. magneta, orange, green, and blue) to improve the spectral resolution of an RGB camera system. Effective observations of rapidly varying processes, such as the aurora, would require simultaneous measurements using several cameras in order to achieve the same results. In this study we have explored the effects of more complex (i.e. multi-notch) filters that modify each RGB channel independently. Our results indicate that these can provide better spectral resolution than a single simple color filter, so that fewer cameras would be required to achieve the desired resolution.

We have also shown that the spectral response of a system consisting of three color CCDs with two modulated filters could be significantly better than a double- or single-camera system. Since this approach is essentially a spectral decomposition using quasi-orthogonal functions, it is tempting to expect that arbitrarily good spectral resolution could be obtained with a sufficiently large number of cameras with different filters. In practice, high-order "spectral synthesis" would be very sensitive to measurement noise, and critically dependent on precise determination of the different measurement kernels. Multiple wide-band color mosaic camera systems will never be functionally equivalent to a single narrow-band device, but they can provide significantly more information than can be obtained with a single color imager, which is in turn more versatile than a white-light device.

The issues that must be considered for field operation of a multiple camera system can be usefully assigned to three different groups. The first set of requirements are essentially identical to those for a single imager i.e. heated building with observing dome, electrical power, and network link. The second set consists of issues that scale linearly with number of cameras N i.e. two cameras will cost twice as much, occupy

GID
3, 753–823, 2013

twice the space under the dome, and produce double the volume of data compared to a single camera. The third set consists of issues unique to a spectral synthesis system, such as orientation, timing, and calibration. It is obviously important that all cameras share a common field of view, but it is relatively easy to achieve this to within 1° by using a single mounting frame, and more precise alignment can be produced in software using star frames. Millisecond timing accuracy is usually possible with available computers and operating systems, so exposures on the order of one second can be considered to be effectively simultaneous for all but the most dynamic aurora. Calibration is likely to be the most difficult issue, as synthesis depends critically on accurate knowledge of the measurement kernels.

The relative response of different channels on a single CCD can easily be determined with a single wavelength scan, but absolute photometry is essential in order to combine data from different instruments. This requires a more complex calibration procedure than used in this study, but is certainly feasible for experienced personnel with a well-equipped dark-room (e.g. Sigernes et al., 2009). Ongoing monitoring of photometric stability could be carried out using stellar sources, and periodic tests carried out with a field calibration source. This level of effort is rarely justified for a single inexpensive camera, but is not unusual for a high-end multi-channel narrow-band system, and could easily be applied to a spectral synthesis system.

The Backus–Gilbert formalism provides an extremely convenient way to analyze the general problem of spectral estimation from a limited set of noisy wide-band measurements. However, it may be useful to consider modifications or alternate (i.e. non-linear) approaches. This suggestion is motivated by the poor results we obtained when considering the entire spectrum (i.e. no hot mirror). Both the H9C and MX7C-fast mode window functions were highly distorted by the influence of similar NIR sensitivity across all channels. Of course, this behavior is an inevitable response of the analysis algorithm to partially non-orthogonal kernels, and reflects a fundamental lack of information relative to the MX7C-raw mode. Still, it might be interesting to explore the effects of altering the definition of “spread” (Eq. 14) to reduce weighting for out-of-band contributions.

GID
3, 753–823, 2013

It may also be productive to define the problem more broadly, not just in terms of color channel observations produced by spectral luminosity $s(\lambda)$, but considering the underlying cause: precipitating electrons and ions with a range of energies incident on a realistic atmosphere with parameters p_k.

$$c_j = F[s(\lambda)] = G[n_e(v), n_i(v); p_1, \ldots, p_k] \quad (25)$$

It is of course unreasonable to expect that a few wide-band color channels will be sufficient to invert G and precisely determine the plasma distribution functions $n(v)$. However, a physically appropriate parametrization may result in a tractable problem that could be used to retrieve valuable information about precipitation characteristics. In a follow-up study we intend to model wide-band response to monoenergetic precipitation and explore the potential for quantitative inversion of color mosaic imager data.

5 Conclusions

Low-cost color mosaic imagers can effectively resolve 3 relatively wide-band channels that are well suited for auroral studies. A color imager has the capability to provide more information than a single channel white-light system, albeit with reductions in sensitivity and resolution that are relatively minor given existing technology. Although spectral resolution is markedly inferior to cameras using narrow-band interference filters, a color mosaic system can provide truly simultaneous acquisition of multiple channels, which may be important for observing dynamic aurora. Consumer grade systems can be obtained with shorter lead times, require lower levels of funding, and are typically easier to operate. Multiple low-cost devices can also be operated at numerous locations to study spatial scales that are inaccessible to a single camera.

Combinations of inexpensive color imagers and structured multi-band filters may be used to achieve significantly improved spectral resolution. Practical application of this spectral synthesis approach will depend critically on the availability of appropriate

GID
3, 753–823, 2013

filters, and the accuracy of filter and CCD calibration. Further work is also necessary to determine the scientific benefits of increased resolution.

Color imagers are increasingly widely used in auroral studies, with more than a dozen systems currently in operation. Although their application thus far has been primarily qualitative, they have significant potential for quantitative spectral analysis. While they are unlikely to replace narrow band systems for auroral spectroscopy, color mosaic cameras have an important role to play in advancing our understanding of ionospheric and magnetospheric processes.

Appendix A

Interline interlaced CCD

The Sony ICX429AKL CCD has a standard rectangular array of photosensitive pixels, arranged as in Fig. A1. An additional matrix of wide-band filters provides the ability to produce color images. This CCD is a interline-transfer device with opaque storage registers located between pixel columns. During readout the pixel array contents are shifted very rapidly into the vertical registers, followed by the slower standard sequence of vertical and horizontal clocking. An interline system is sometimes referred to as having an "electronic shutter", as it essentially eliminates image smearing during readout.

The ICX429AKL uses an interlaced readout, meaning that an interline shift can be applied to even or odd rows separately. Either case produces an image frame that has half the vertical resolution of the native ("raw") CCD. The full resolution can be acquired by reading the even and odd frames successively, but the two frames will correspond to different time intervals. An alternative "fast" mode readout applies an interline shift to both the even and odd rows, but vertical pairs of pixels are combined in a single vertical register, so colors are mixed and vertical resolution is irreversibly halved. In return this mode provides a simultaneous exposure of all image pixels that is not susceptible to time variations in brightness or spectral content.

GID
3, 753–823, 2013

It is useful to compare the different readout options in quantitative terms. One obvious metric is duty cycle: the maximum fraction of time that can be spent acquiring photons, with higher duty cycle allowing higher sensitivity. For time varying sources we also care about simultaneity: the amount of overlap between even and odd frames.

The "fast" mode (Fig. A2a) exposes both even and odd rows simultaneously for an interval T, combining and reading them out over a time t. Effective duty cycle of $\eta = T/(T+t)$ could approach 100 % for $T \gg t$. Sensitivity results presented in this study were obtained using the non-overlapping sequence shown in Fig. A2b with a maximum duty cycle $\eta = T/(2T+t)$ less than 50 %. Low duty cycle and complete lack of simultaneity are not issues for stable calibration, but can be significant concerns for auroral observations. The timing sequence in Fig. A2c provides a maximal duty cycle $\eta = T/(T+t)$ but with an overlap $\beta = (T-t)/2T$ of less than 50 %. The best-case "pseudo-progressive" exposure sequence in Fig. A2d maximises duty cycle and overlap $\beta = (T-t)/T$.

The nearly optimal timing sequence in Fig. A2d would produce nearly simultaneous even and odd frames that are shifted by the relatively short readout time t. Using the electronic shutter capability it may be possible to (1) start exposing the entire CCD, (2) wait for an interval t then clear and resume exposing the odd frame, (3) finish exposing the even frame and read it out, (4) finish exposing the odd frame and read it out. This timing sequence would require precise timing control to ensure that even and odd frames were consistently exposed for equal amounts of time.

Appendix B

Sony ICX429AKL YUV/RGB

The color processing method outlined in the ICX429AKL CCD data sheet (Sony, 2003) uses data from the "fast" readout mode to construct a YUV (luma/chroma) signal. The data sheet does not indicate the specific conversion process from YUV to RGB, so for

GID
3, 753–823, 2013

simplicity we will use definitions from (International Telecommunication Union, 2011, BT601) Sect. 2.5

$$Y \equiv +0.299\mathrm{R} + 0.587\mathrm{G} + 0.114\mathrm{B} \quad [0.0, 1.0] \tag{B1a}$$

$$U \equiv B - Y = -0.299\mathrm{R} - 0.587\mathrm{G} + 0.886\mathrm{B} \quad [\mp 0.886] \tag{B1b}$$

$$V \equiv R - Y = +0.701\mathrm{R} - 0.587\mathrm{G} - 0.114\mathrm{B} \quad [\mp 0.701] \tag{B1c}$$

where by convention RGB values are scaled to be in the range 0 to 1, producing YUV values between the ranges shown in Eq. (B1). The corresponding inverse transformation from YUV to RGB is given by

$$\mathrm{R} = +1.0Y + 0.0U + 1.0V \quad [0.0, 1.0] \tag{B2a}$$

$$\mathrm{G} = +1.0Y - 0.194U - 0.509V \quad [0.0, 1.0] \tag{B2b}$$

$$\mathrm{B} = +1.0Y + 1.0U + 0.0V \quad [0.0, 1.0] \tag{B2c}$$

In general it is necessary to consider gamma corrected quantities (R′, G′, B′, Y′), but for this particular case we simplify matters by using $\gamma = 1$.

At this point it is convenient to introduce "starred" (e.g. Y^*) notation to represent quantities that are in the pixel count range $[0, N_{\mathrm{max}}]$. Summing horizontally adjacent pixels from ICX429AKL fast mode data will provide estimates of the brightness (luminance) Y^*

$$Y^* = (\mathrm{Gr} + \mathrm{Cy})^* + (\mathrm{Mg} + \mathrm{Ye})^* \sim 2\mathrm{B}^* + 3\mathrm{G}^* + 2\mathrm{R}^* \tag{B3}$$

while subtracting horizontally adjacent pixels will provide estimates of the color difference (chrominance) channels U^* and V^*

$$U^* = (\mathrm{Mg} + \mathrm{Cy})^* - (\mathrm{Gr} + \mathrm{Ye})^* \sim 2\mathrm{B}^* - \mathrm{G}^* \tag{B4}$$

$$V^* = (\mathrm{Mg} + \mathrm{Ye})^* - (\mathrm{Gr} + \mathrm{Cy})^* \sim 2\mathrm{R}^* - \mathrm{G}^* \tag{B5}$$

GID
3, 753–823, 2013

with different equations applied to the even and odd rows. A 2×2 pixel block of fast mode data will be sufficient to determine both U^* and V^*, along with two independent luminance estimates Y_1^* and Y_2^*.

$$\begin{bmatrix} Y_1 \\ Y_2 \\ U \\ V \end{bmatrix}^* = \begin{bmatrix} \frac{1}{2} & \frac{1}{2} & 0 & 0 \\ 0 & 0 & \frac{1}{2} & \frac{1}{2} \\ +1 & -1 & 0 & 0 \\ 0 & 0 & +1 & -1 \end{bmatrix} \begin{bmatrix} \mathrm{Gr} + \mathrm{Ye} \\ \mathrm{Mg} + \mathrm{Cy} \\ \mathrm{Mg} + \mathrm{Ye} \\ \mathrm{Gr} + \mathrm{Cy} \end{bmatrix}^* \tag{B6}$$

De-mosaicing considerations are neglected in this study, so we assume equality of the luminance estimates

$$Y^* = \frac{1}{2}(Y_1^* + Y_2^*) \approx Y_1^* \approx Y_2^* \tag{B7}$$

which can be conveniently expressed in matrix notation

$$\begin{bmatrix} Y \\ U \\ V \end{bmatrix}^* = \begin{bmatrix} \frac{1}{2} & \frac{1}{2} & 0 & 0 \\ 0 & 0 & 1 & 0 \\ 0 & 0 & 0 & 1 \end{bmatrix} \begin{bmatrix} Y_1 \\ Y_2 \\ U \\ V \end{bmatrix}^* \tag{B8}$$

Using fast-mode response curves from Fig. 7 produces YUV spectral calibration results shown in Fig. A3a. These can be used to rescale pixel count-based $Y^*U^*V^*$ values onto the normalized ranges for YUV given in Eq. (B1)

$$\begin{bmatrix} Y \\ U \\ V \end{bmatrix} = \begin{bmatrix} s_1 & 0 & 0 \\ 0 & s_2 & 0 \\ 0 & 0 & s_3 \end{bmatrix} = \begin{bmatrix} Y^* \\ U^* \\ V^* \end{bmatrix} \tag{B9}$$

with empirically determined scaling factors of Fig. A3

$$(s_1, s_2, s_3) \approx \frac{1}{N_{\max}} \left(\frac{1}{1.3}, \frac{0.886}{0.45}, \frac{0.701}{0.45} \right) \tag{B10}$$

GID
3, 753–823, 2013

to get a direct mapping from fast-mode pixel counts to $R^*G^*B^*$ (scaled from 0 to N_{max}) as shown in Fig. A3b.

$$\begin{bmatrix} R \\ G \\ B \end{bmatrix}^* = \begin{bmatrix} +0.1923 & +0.1923 & +1.7501 & -1.3655 \\ -0.1897 & +0.5743 & -0.6006 & +0.9852 \\ +2.1612 & -1.7766 & +0.1923 & +0.1923 \end{bmatrix} \begin{bmatrix} Gr + Ye \\ Mg + Cy \\ Mg + Ye \\ Gr + Cy \end{bmatrix}^* \quad \text{(B11)}$$

Acknowledgements. Operational support for the Canadian Rainbow network was provided by the Canadian Space Agency. Linux kernel camera driver software was written by David Schmenk. AURIC auroral spectra were provided by Scott Evans at Computational Physics Incorporated.

References

Aster, R. C., Borchers, B., and Thurber, C. H.: Parameter Estimation and Inverse Problems, Elsevier, Burlington, MA, USA, 2005. 769, 771

Backus, G. and Gilbert, F.: The resolving power of gross Earth data, Geophys. J. Roy. Astr. S., 16, 169–205, doi:10.1111/j.1365-246X.1968.tb00216.x, 1968. 771

Backus, G. and Gilbert, F.: Uniqueness in the inversion of inaccurate gross Earth data, Philos. T. R. Soc. S. A, 266, 123–192, 1970. 771

Dahlgren, H., Ivchenko, N., Sullivan, J., Lanchester, B. S., Marklund, G., and Whiter, D.: Morphology and dynamics of aurora at fine scale: first results from the ASK instrument, Ann. Geophys., 26, 1041–1048, doi:10.5194/angeo-26-1041-2008, 2008. 756, 778

Donovan, E. F., Mende, S., Jackel, B. J., Frey, H., Syrjäsuo, M., Voronkov, I. O., Trondsen, T., Peticolas, L., Angelopoulos, V., Harris, S., Greffen, M., and Connors, M.: The THEMIS all-sky imaging array – system design and initial results from the prototype imager, J. Atmos. Sol.-Terr. Phy., 68, 1472–1487, doi:10.1016/j.jastp.2005.03.027, 2006. 758

Goenka, C., Semeter, J., Noto, J., Dahlgren, H., Marshall, R., Baumgardner, J., Riccobono, J., and Migliozzi, M.: Tunable filters for multispectral imaging of aeronomical features, Adv. Space Res., 52, 1366–1377, doi:10.1016/j.asr.2013.06.014, 2013. 778

GID
3, 753–823, 2013

Gunturk, B., Glotzbach, J., Altunbasak, Y., Schafer, R., and Mersereau, R.: Demosaicking: color filter array interpolation, IEEE Signal Proc. Mag., 22, 44–54, doi:10.1109/MSP.2005.1407714, 2005. 763

Harris, S. E., Mende, S. B., Angelopoulos, V., Rachelson, W., Donovan, E. F., Jackel, B. J., Greffen, M., Russell, C. T., Pierce, D. R., Dearborn, D. J., Rowe, K. M., and Connors, M.: THEMIS ground based observatory system design, Space Sci. Rev., 141, 213–233, doi:10.1007/s11214-007-9294-z, 2008. 758

International Telecommunication Union: Studio encoding parameters of digital television for standard 4 : 3 and wide-screen 16 : 9 aspect ratios (ITU-R B T.601-7), Tech. rep., International Telecommunication Union, Geneva, 2011. 788

López-Alvarez, M. A., Hernández-Andrés, J., and Romero, J.: Developing an optimum computer-designed multispectral system comprising a monochrome CCD camera and a liquid-crystal tunable filter, Appl. Optics, 47, 4381–4390, 2008. 778

Menke, W.: Geophysical Data Analysis: Discrete Inverse Theory, revised Edn., Academic Press, London, UK, 1989. 769, 771

Nieves, J. L., Valero, E. M., Nascimento, S. M. C., Hernández-Andrés, J., and Romero, J.: Multispectral synthesis of daylight using a commercial digital CCD camera, Appl. Optics, 44, 5696–5703, 2005. 757

Nieves, J. L., Valero, E. M., Hernández-Andrés, J., and Romero, J.: Recovering fluorescent spectra with an RGB digital camera and color filters using different matrix factorizations, Appl. Optics, 46, 4144–4154, 2007. 757

Parker, R. L.: Inverse theory with grossly inadequate data, Geophys. J. Int., 29, 123–138, doi:10.1111/j.1365-246X.1972.tb02203.x, 1972. 771

Partamies, N., Syrjäsuo, M., and Donovan, E. F.: Using colour in auroral imaging, Can. J. Phys., 85, 101–109, doi:10.1139/p06-090, 2007. 757, 759

Partamies, N., Syrjäsuo, M., Donovan, E. F., and Knudsen, D. J.: Dense Array Imaging SYstem prototype observations of missing auroral scale sizes, Proceedings of the 33rd Annual Meeting on Atmospheric Studies by Optical Methods, IRF Sci. Rep, 292, 95–101, 2008. 760

Partamies, N., Sangalli, L., Donovan, E., Connors, M., and Charrois, D.: Tomography-like approach for analysing colour auroral images, Geophysica, 48, 81–90, 2012. 757

Pulkkinen, T. I., Janhunen, P., Viljanen, A., Pellinen, R. J., Kauristie, K., Opgenoorth, H. J., Wallman, S., Eglitis, P., Amm, O., Nielsen, E., and Thomas, C.: Observations of substorm

GID
3, 753–823, 2013

electrodynamics using the miracle network, in: Proceedings of the International Conference on Substorms – 4, 238, 111–114, 1998. 759
Rees, M. H. and Luckey, D.: Auroral electron energy derived from ratio of spectroscopic emissions, 1. model computations, J. Geophys. Res., 79, 5181–5186, doi:10.1029/JA079i034p05181, 1974. 754
Rodgers, C. D.: Retrieval of atmospheric temperature and composition from remote measurements of thermal radiation, Rev. Geophys., 14, 609–624, 1976. 769
Rodgers, C. D.: Characterization and error analysis of profiles retrieved from remote sounding measurements, J. Geophys. Res., 95, 5587–5595, doi:10.1029/JD095iD05p05587, 1990. 769
Sigernes, F., Holmes, J. M., Dyrland, M., Lorentzen, D. A., Svenøe, T., Heia, K., Aso, T., Chernouss, S., and Deehr, C. S.: Sensitivity calibration of digital colour cameras for auroral imaging, Opt. Express, 16, 15623–15632, 2008. 757, 763
Sigernes, F., Dyrland, M., Peters, N., Lorentzen, D. A., Svenøe, T., Heia, K., Chernouss, S., Deehr, C. S., and Kosch, M.: The absolute sensitivity of digital colour cameras, Opt. Express, 17, 20211–20220, doi:10.1364/OE.17.020211, 2009. 757, 763, 784
Sigernes, F., Ivanov, Y., Chernouss, S., Trondsen, T., Roldugin, A., Fedorenko, Y., Kozelov, B., Kirillov, A., Kornilov, I., Safargaleev, V., Holmen, S., Dyrland, M., Lorentzen, D., and Baddeley, L.: Hyperspectral all-sky imaging of auroras, Opt. Express, 20, 27650–27660, 2012. 778
Sony: ICX429AKL color CCD, 2003. 787
Steele, D. P. and Cogger, L. L.: Polar patches and the “tongue of ionization”, Radio Sci., 31, 667–677, doi:10.1029/96RS00369, 1996. 756, 778
Strickland, D. J., Meier, R. R., Hecht, J. H., and Christensen, A. B.: Deducing composition and incident electron spectra from ground-based auroral optical measurements: theory and model results, J. Geophys. Res., 94, 13527–13539, doi:10.1029/JA094iA10p13527, 1989. 754
Strickland, D., Bishop, J., Evans, J., Majeed, T., Shen, P. M., Cox, R. J., Link, R., and Huffman, R. E.: Atmospheric Ultraviolet Radiance Integrated Code (AURIC): theory, software architecture, inputs, and selected results, J. Quant. Spectrosc. Ra., 62, 689–742, 1999. 755
Tarantola, A.: Inverse Problem Theory and Methods for Model Parameter Estimation, vol. 130, Society for Industrial and Applied Mathematics, Philadelphia, avail-

GID
3, 753–823, 2013

able at: http://www.ipgp.fr/~tarantola/Files/Professional/Teaching/Diverse/Complements_2/Lessons/Lessons_1-3.pdf (last access: 7 December 2013), 2005. 769

Toyomasu, S., Futaana, Y., Yamauchi, M., and Turiststation, A.: Low cost webcast system of real-time all-sky auroral images and MPEG archiving in Kiruna, in: Proceedings of 33rd Annual European Meeting on Atmospheric Studies by Optical Methods, Kiruna, 292, 75–84, available at: http://www.irf.se/publications/proc33AM_files/toyomasu-etal.pdf (last access: 7 December 2013), 2008. 756

Valero, E. M., Nieves, J. L., Nascimento, S. M. C., Amano, K., and Foster, D. H.: Recovering spectral data from natural scenes with an RGB digital camera and colored filters, Color Res. Appl., 32, 352–360, doi:10.1002/col.20339, 2007. 783

Wyszecki, G. and Stiles, W. S.: Color science: concepts and methods, quantitative data and formulae, 2nd Edn., Wiley-Interscience, New York, 2000. 775

GID

3, 753–823, 2013

Table 1. Commonly studied visible auroral wavelengths.

λ [nm]	source
391.4	N_2^+ 1NG(0,0)
427.8	N_2^+ 1NG
470.9	N_2^+ 1NG
486.1	H_β
557.7	$O(^1D–^3P_2)$
630.0	$O(^1D \rightarrow {}^1S)$
656.3	H_α
777.4	OI
844.6	OI

GID
3, 753–823, 2013

Table 2. Location of auroral all-sky color imaging systems. Geographic latitude and longitude are in degrees north and east respectively.

site	geographic		device	operating
ID	lat	lon	type	dates
Calgary				
FSIM	61.43	−121.17	mx7c	Nov 2006–Apr 2013
FSMI	59.98	−111.84	mx7c	Noc 2009–Apr 2013
GILL	56.38	−94.64	mx7c	Sep 2010–Apr 2013
PINA	50.20	−96.08	mx7c	Sep 2009–Sep 2010
RABB	58.17	−103.66	mx7c	Oct 2006–Feb 2013
RESU	74.73	−94.97	mx7c	Nov 2007–Nov 2012
SASK	52.12	−107.07	mx7c	Sep 2008–Feb 2013
YKNF	62.52	−114.31	h9c	Mar 2009–Apr 2013
Miracle				
NYR	62.34	−25.51	mx7c	May 2005–May 2013
KEV	69.76	−27.01	mx7c	Dec 2007–May 2013
MUO	68.02	−23.53	mx7c	Dec 2007–May 2013
HEL	60.17	−24.93	mx7c	Sep 2009–May 2013
Lancaster				
HSRN	62.02	−6.83	mx7c	Oct 2009–Aug 2012
PYKK	63.77	−20.54	mx7c	Oct 2007–Feb 2011
TJRN	66.20	−17.10	mx7c	Sep 2009–Mar 2012
SRI				
SND	67	51	mx7c	Oct 2008–May 2013
UCL				
SOD	67.37	−26.63	h9c	Sep 2007–May 2013
KHO	78.15	−16.04	h9c	Sep 2007–May 2013
KEOPS	67.88	−21.07	mx7c	Jan 2002–Feb 2012

GID
3, 753–823, 2013

Table 3. Characteristics of two color mosaic CCDs.

Sony model	ICX429AKL	ICX285AQ
optical size	8 mm diagonal	11 mm diagonal
chip size (HxV) [mm]	7.40 × 5.96	10.2 × 8.3
pixels (effective)	752 × 582	1392 × 1040
unit cell size [µm]	8.6 × 8.3	6.45 × 6.45
readout mode	interlaced	progressive
color mosaic	YeCyMgGr	RGB
Starlight-Xpress model	MX7-C	SXV-H9C

GID
3, 753–823, 2013

Table 4. Noise sensitivity as indicated by the RMS value of coefficients in **D** matrix rows.

	R	G	B
H9C	0.2809	0.6645	1.0000
fast	0.1833	0.5052	1.3568
raw	0.2810	0.5458	1.3978

GID
3, 753–823, 2013

Table 5. Average spread, error, and noise over the wavelength range 450–650 nm for different cameras and filter combinations.

	spread [nm]	error	bias [nm]
7f	202.1	0.0248	29.8
7p	97.6	0.1001	5.7
9	127.3	0.0144	19.8
79	86.5	0.0374	12.2
7n	181.8	0.0350	29.3
7m	127.2	0.1505	14.3
7mm	76.3	0.1387	8.7

GID
3, 753–823, 2013

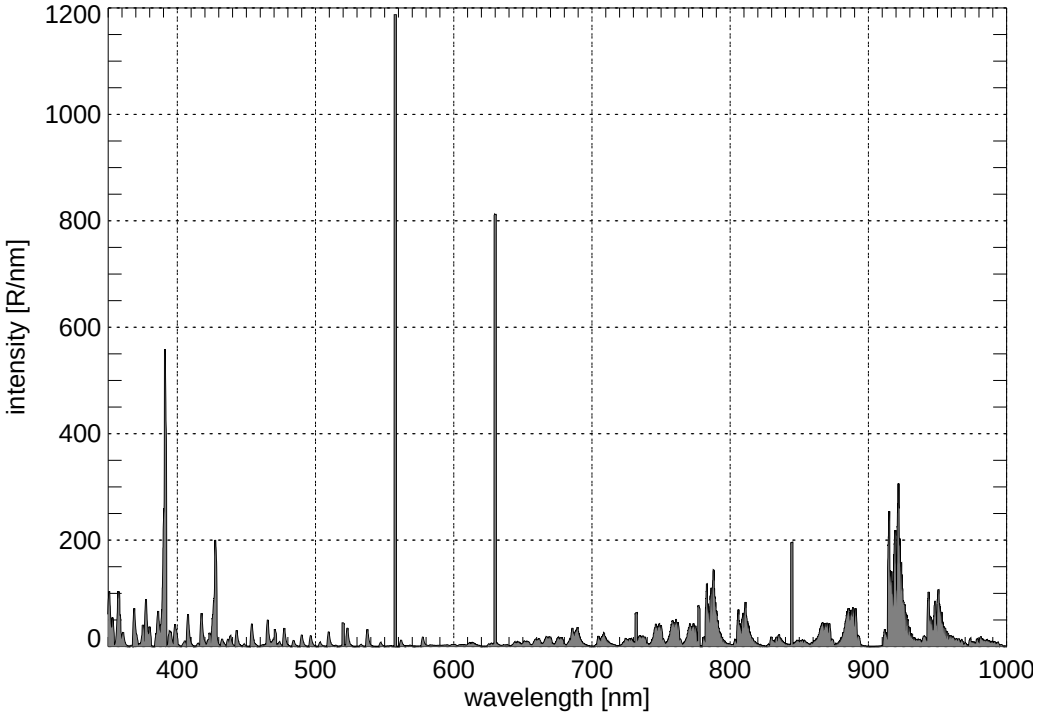

Fig. 1. Auroral spectrum during low activity geomagnetic and solar conditions for a beam of 1 keV monoenergetic electrons with a total energy flux of 1 mW m^{-2}.

GID
3, 753–823, 2013

Wide band color CCD spectral estimation

B. J. Jackel et al.

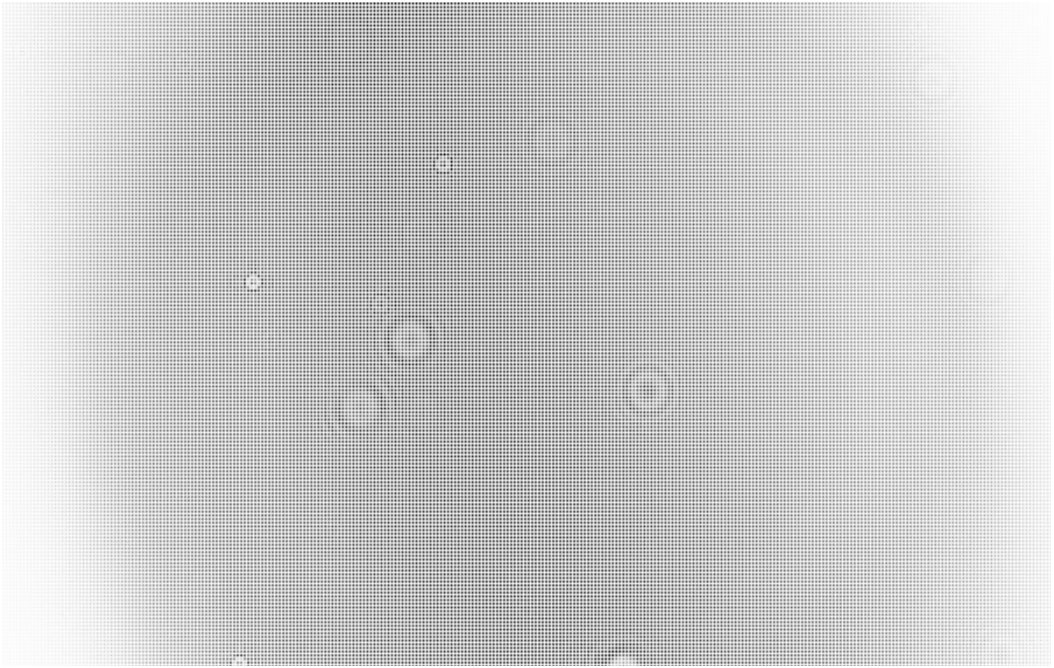

Fig. 2. Contrast enhanced sub-region of ICX285AQ calibration frame at 600 nm. Fine grid pattern produced by Bayer mosaic response to monochromatic light, coarse grid is moiré artifact.

GID
3, 753–823, 2013

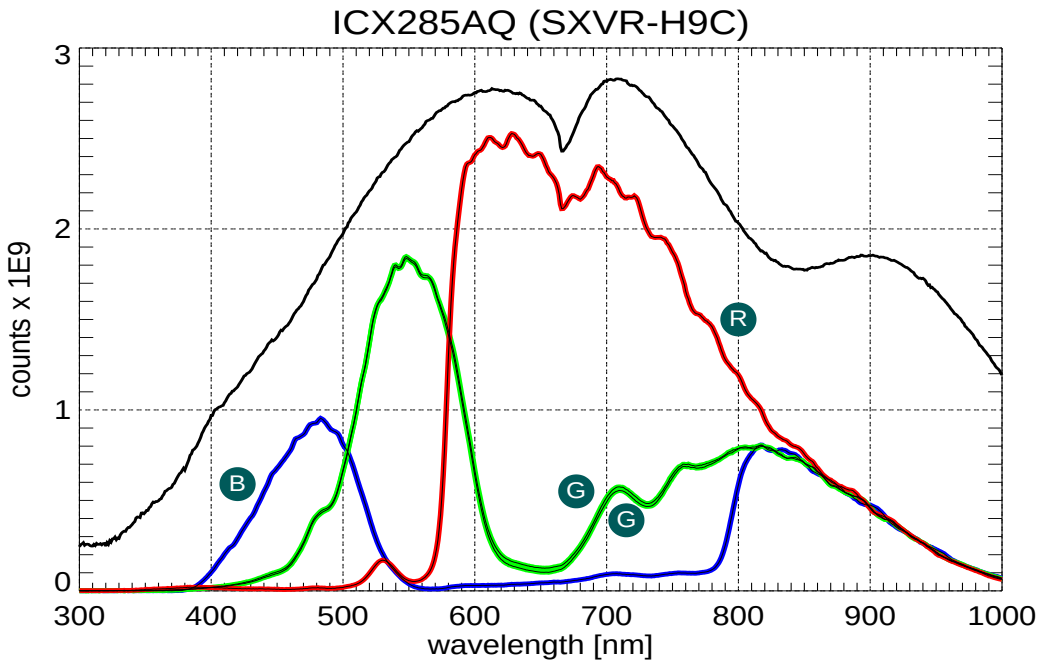

Fig. 3. Sony ICX285AQ calibration counts and reference diode power level. Letters indicate the four channels: blue, red, and two nearly identical green.

GID
3, 753–823, 2013

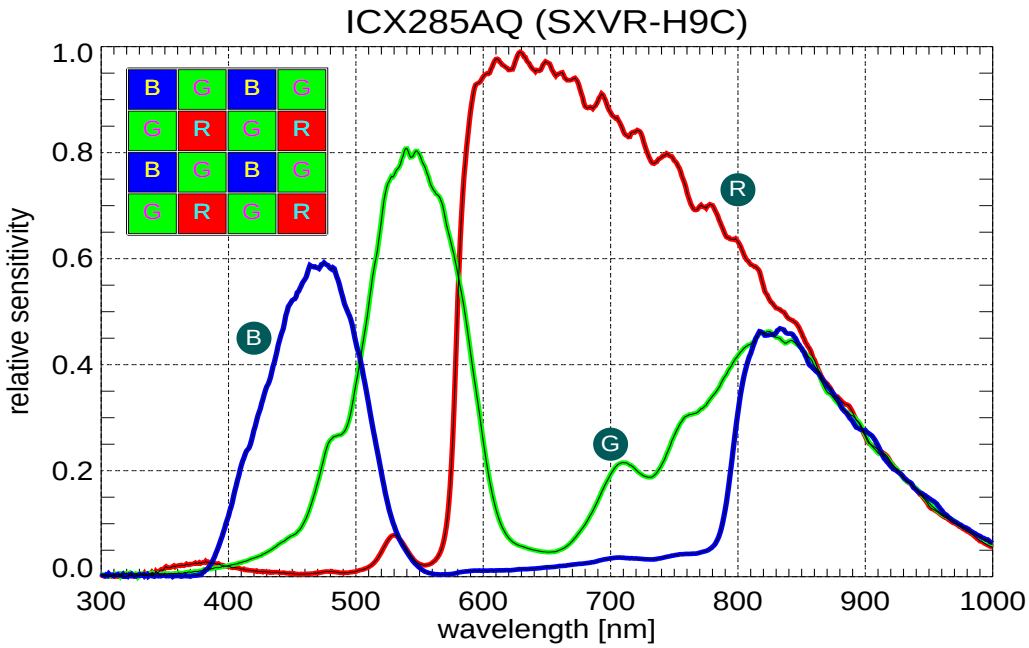

Fig. 4. Spectral response for three channel (RGB) Sony ICX285HQ CCD with Bayer color mosaic inset.

GID
3, 753–823, 2013

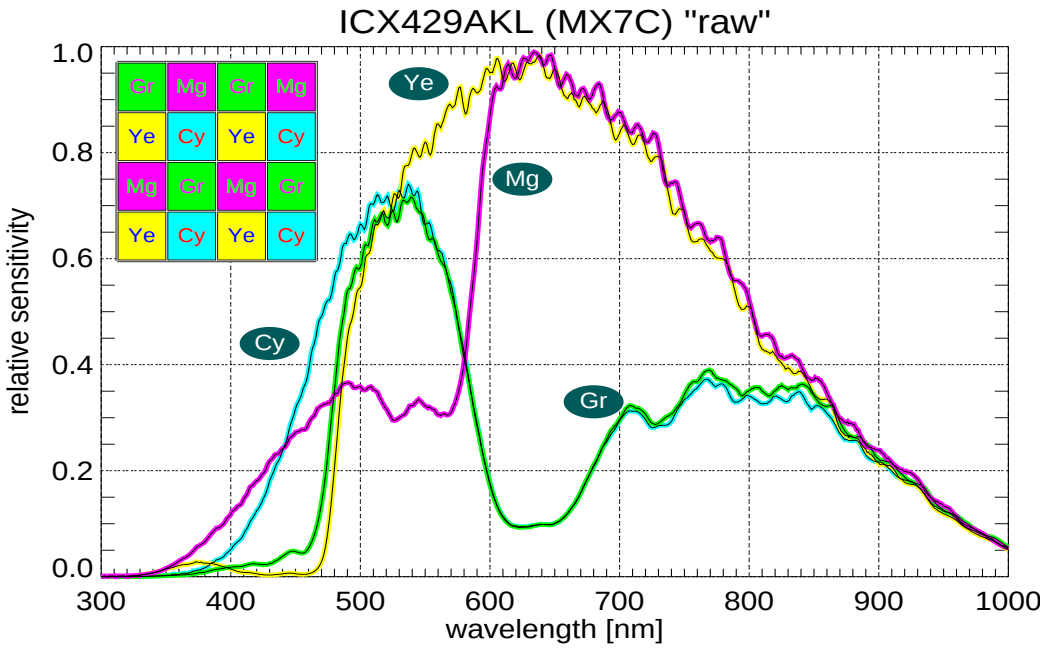

Fig. 5. Spectral response of four channel (CYGM) Sony ICX429AKL CCD in “raw” mode with color mosaic inset.

GID
3, 753–823, 2013

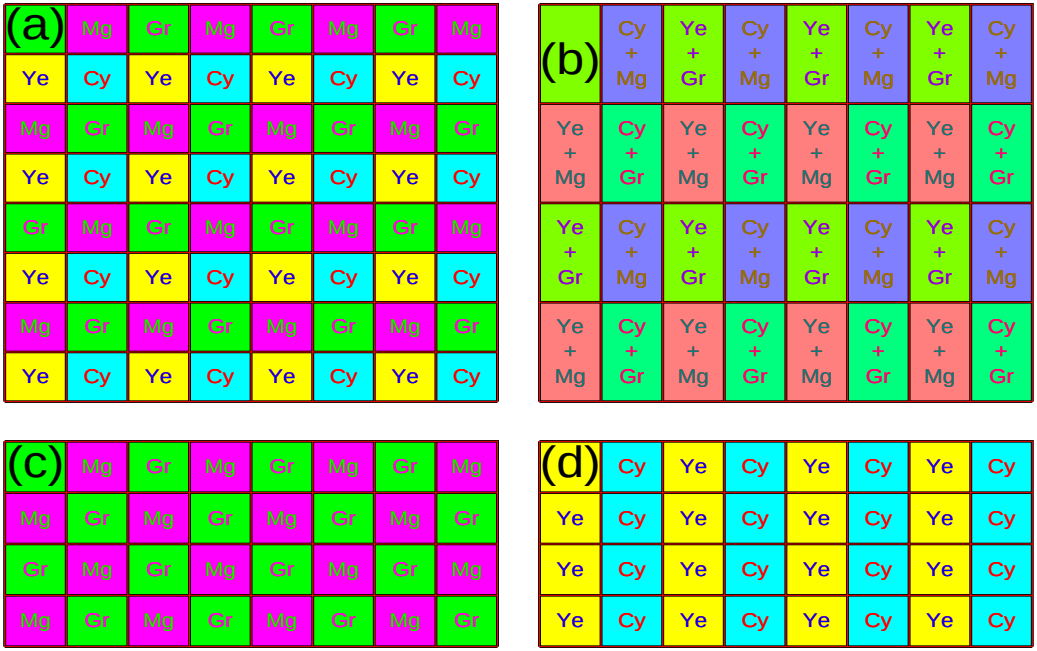

Fig. 6. Sony ICX429AKL **(a)** "raw" full color mosaic, **(b)** "fast" binned row pairs, **(c)** even rows, and **(d)** odd rows.

GID
3, 753–823, 2013

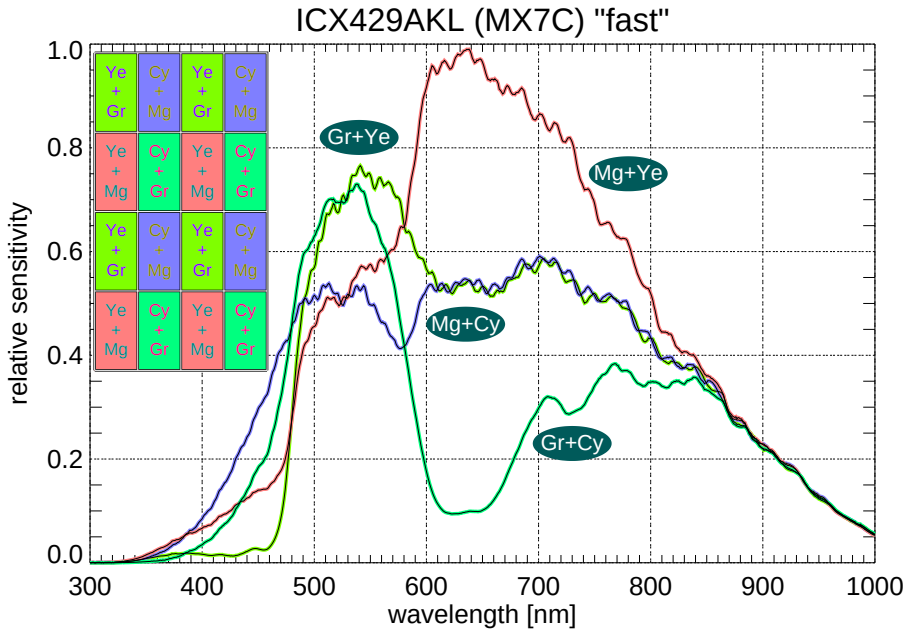

Fig. 7. Spectral response of four channel (CYGM) Sony ICX429AKL CCD in “fast” mode.

GID
3, 753–823, 2013

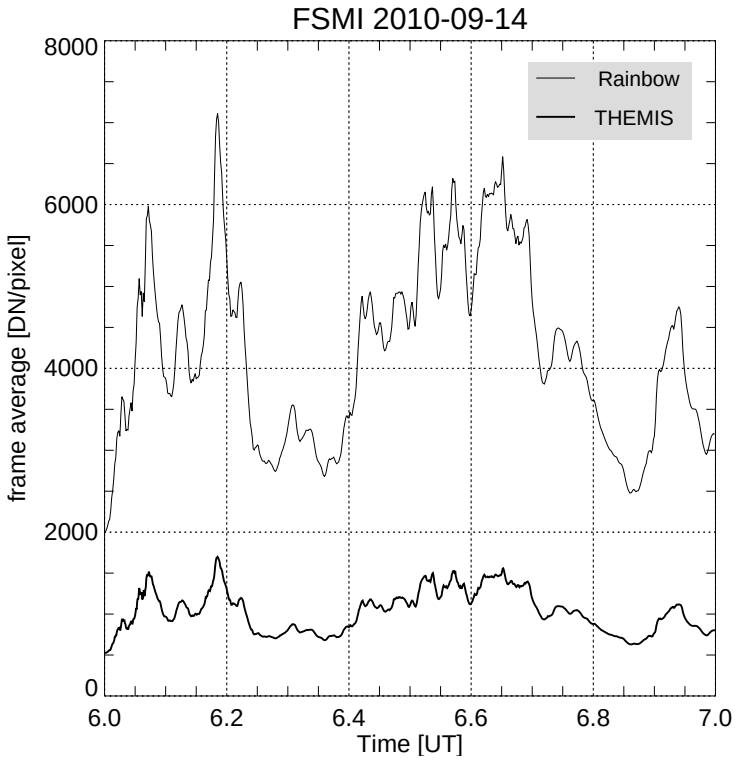

Fig. 8. Response of co-located Rainbow and THEMIS imagers at Fort Smith during an active period from 06:00–07:00 UT on 14 September 2010. Frame average counts are divided by exposure times of 1 s for THEMIS and 5 s for Rainbow to produce comparable rates. THEMIS data are plotted at 3 s intervals and Rainbow at 6 s intervals; timing differences are not visible on this one hour interval. Results are very highly correlated ($r^2 \approx 0.994$) with a ratio of 87 %.

GID
3, 753–823, 2013

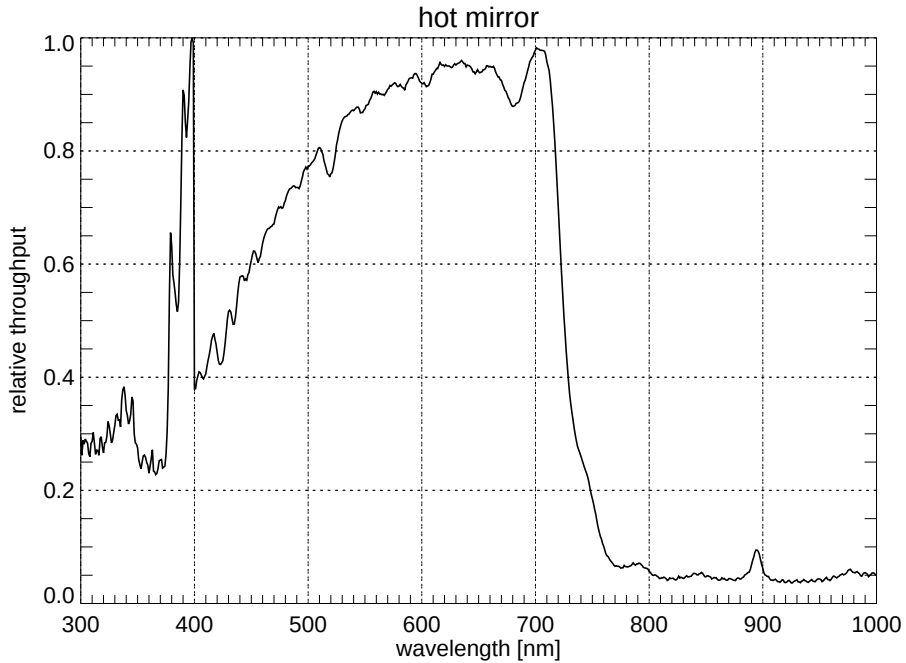

Fig. 9. Transmission for infra-red blocking filter ("hot mirror") used in THEMIS and Rainbow cameras. Feature at 380–400 nm is a calibration artifact that does not significantly effect analysis results.

GID
3, 753–823, 2013

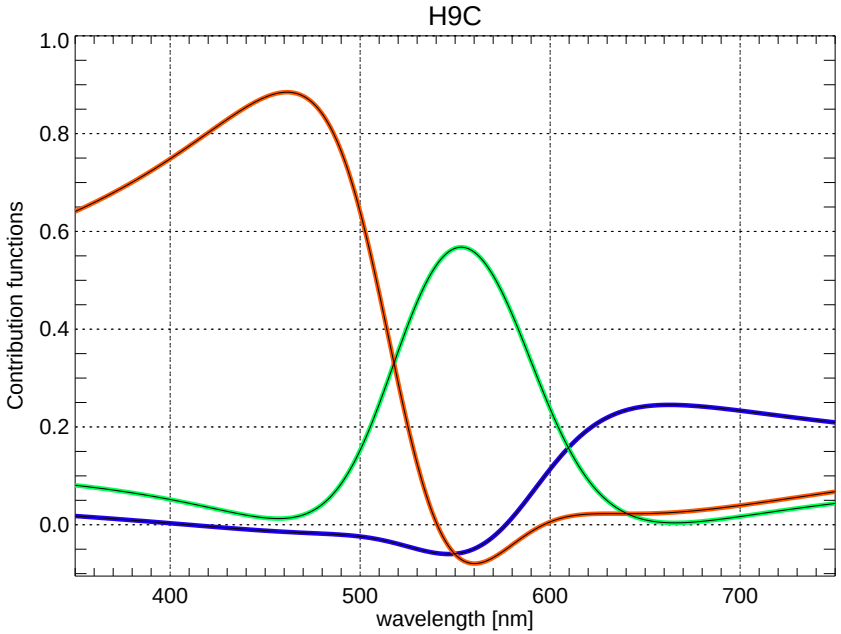

Fig. 10. Contribution functions (D) for the ICX285AQ with smoothing parameter $\mu = 1$.

GID
3, 753–823, 2013

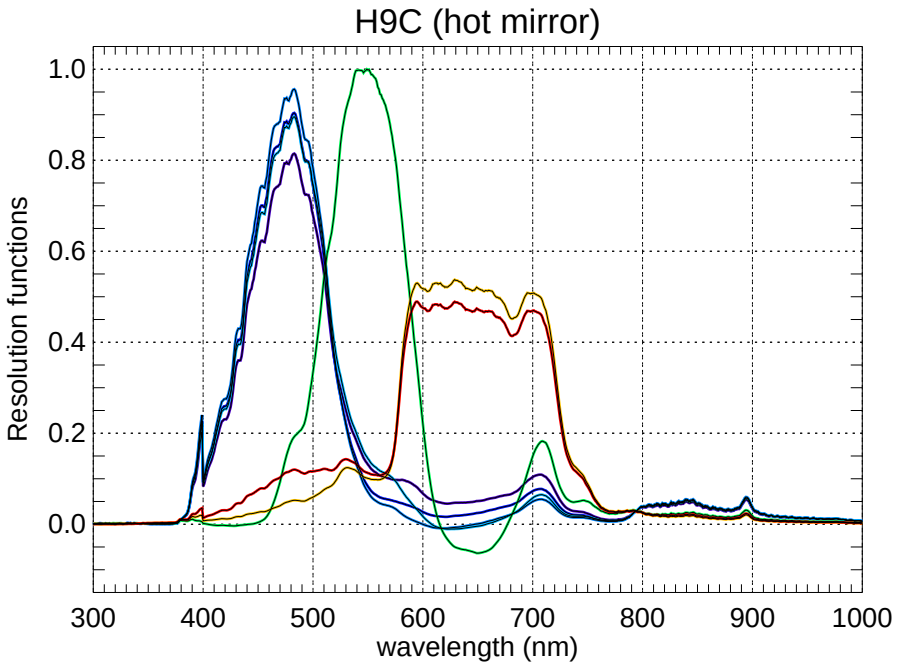

Fig. 11. Resolution/window functions (A) for ICX285AQ with smoothing parameter $\mu = 1$ and retrieved wavelengths of 391.4 nm (dark blue), 427.8 nm (blue), 470.9 nm (light blue), 486.1 nm (cyan), 557.7 nm (green), 630.0 nm (orange), and 777.7 nm (red).

GID
3, 753–823, 2013

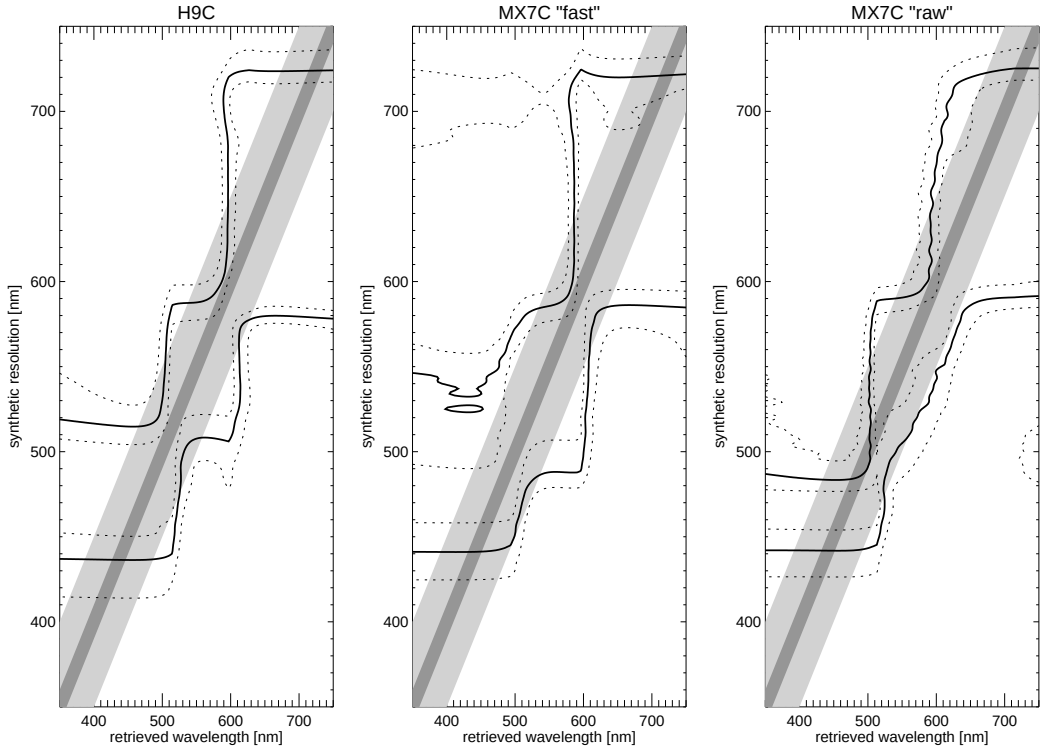

Fig. 12. Contour plots of resolution function (y axis) variation with retrieved wavelength (x axis). All functions are normalized to unit peak; full-width half-maximum (FWHM) is indicated by the solid contour. Light and dark diagonal shading corresponds to an unbiased detector with FWHM = 100 nm and 20 nm respectively.

GID
3, 753–823, 2013

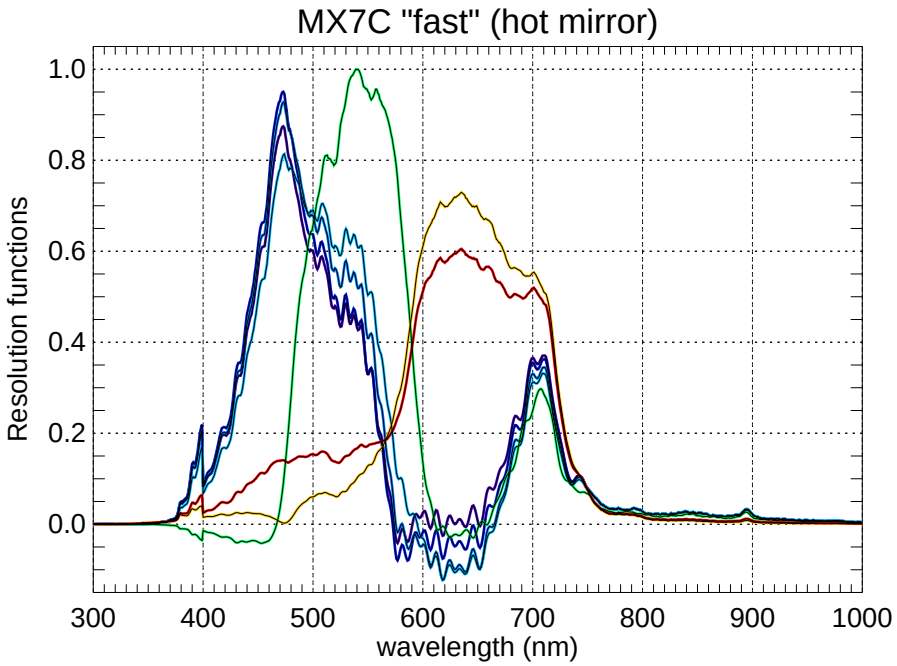

Fig. 13. Resolution/window functions (A) for ICX429AKL in "fast" mode with smoothing μ = 1 and retrieved wavelengths of 391.4 nm (dark blue), 427.8 nm (blue), 470.9 nm (light blue), 486.1 nm (cyan), 557.7 nm (green), 630.0 nm (orange), and 777.7 nm (red).

GID
3, 753–823, 2013

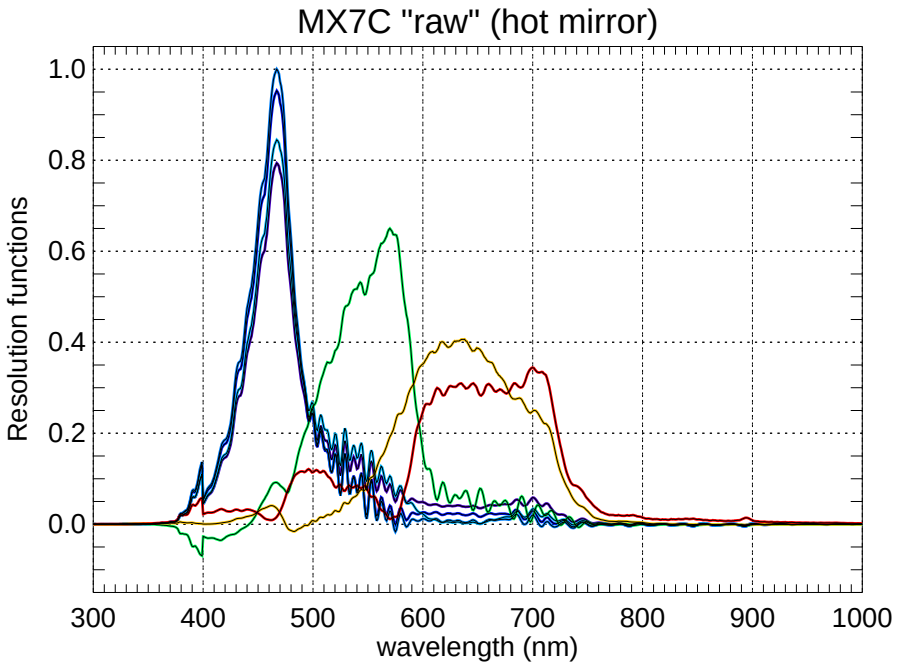

Fig. 14. Resolution/window functions (A) for ICX429AKL in "raw" mode with smoothing μ = 1 and retrieved wavelengths of 391.4 nm (dark blue), 427.8 nm (blue), 470.9 nm (light blue), 486.1 nm (cyan), 557.7 nm (green), 630.0 nm (orange), and 777.7 nm (red).

GID
3, 753–823, 2013

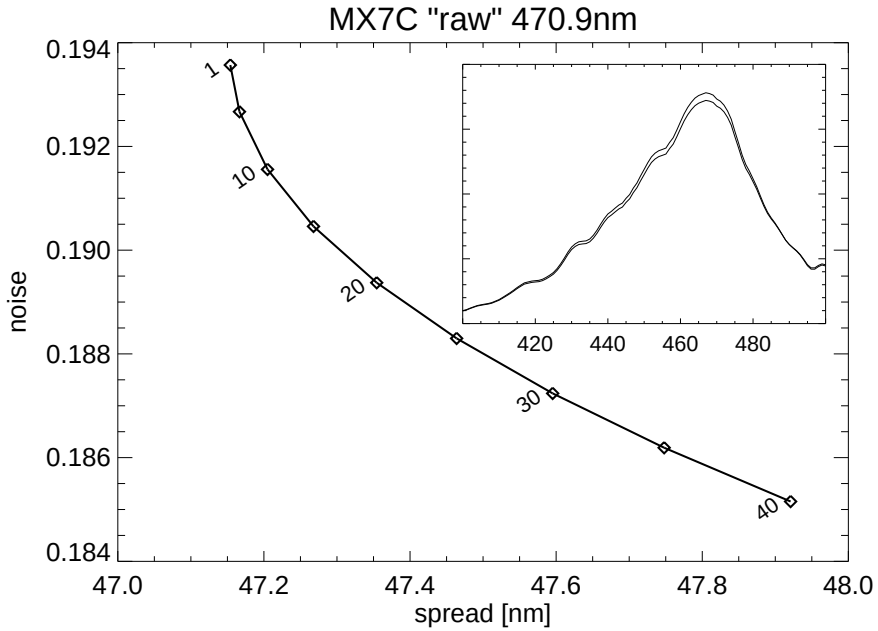

Fig. 15. Backus–Gilbert trade-off curve with inverse relationship between resolution function spread and retrieval error. Results were obtained using MX7C "raw" kernels with a retrieval wavelength of 470.9 nm and μ ranging from 1 to 40. Inset shows nearly indistinguishable resolution functions for $\mu = 1$ and $\mu = 40$.

GID
3, 753–823, 2013

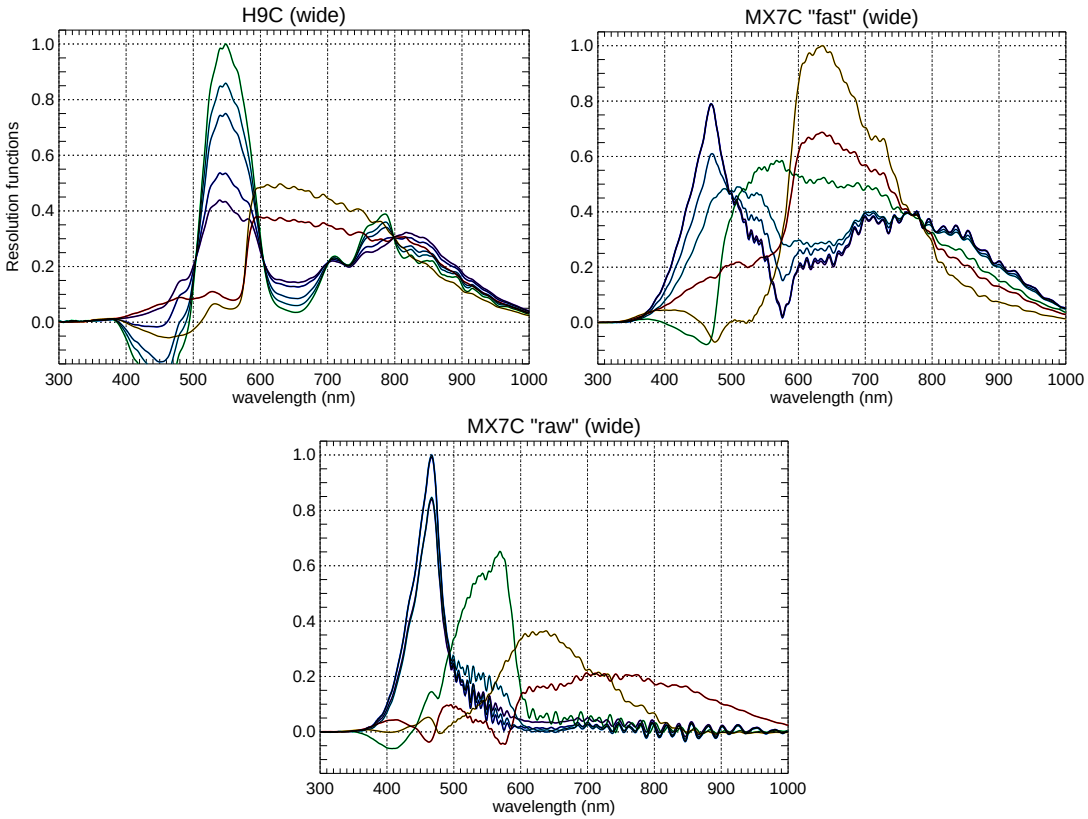

Fig. 16. Resolution/window functions (*A*) without infra-red blocking "hot mirror".

GID
3, 753–823, 2013

Wide band color CCD spectral estimation

B. J. Jackel et al.

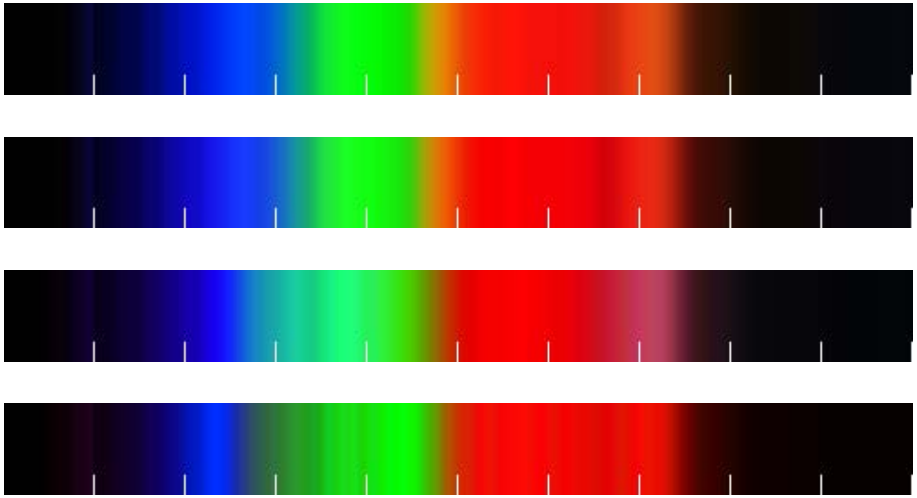

Fig. 17. Color bars for calibration wavelengths from 350 nm to 850 nm with tickmarks at 50 nm intervals. Top bar **(a)** is direct mapping of ICX285HQ Bayer matrix to RGB. Lower three are Backus–Gilbert estimation of CIE RGB channels for **(b)** ICX285HQ, **(c)** ICX429AKL fast mode, and **(d)** ICX429AKL raw mode.

GID
3, 753–823, 2013

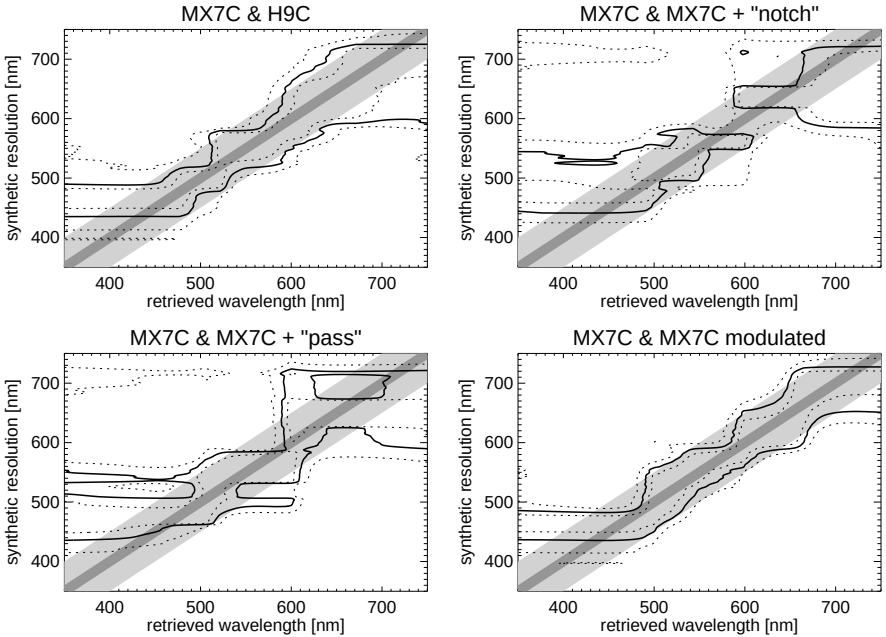

Fig. 18. Backus–Gilbert spectral response analysis for combinations of two color CCDs and filters.

GID
3, 753–823, 2013

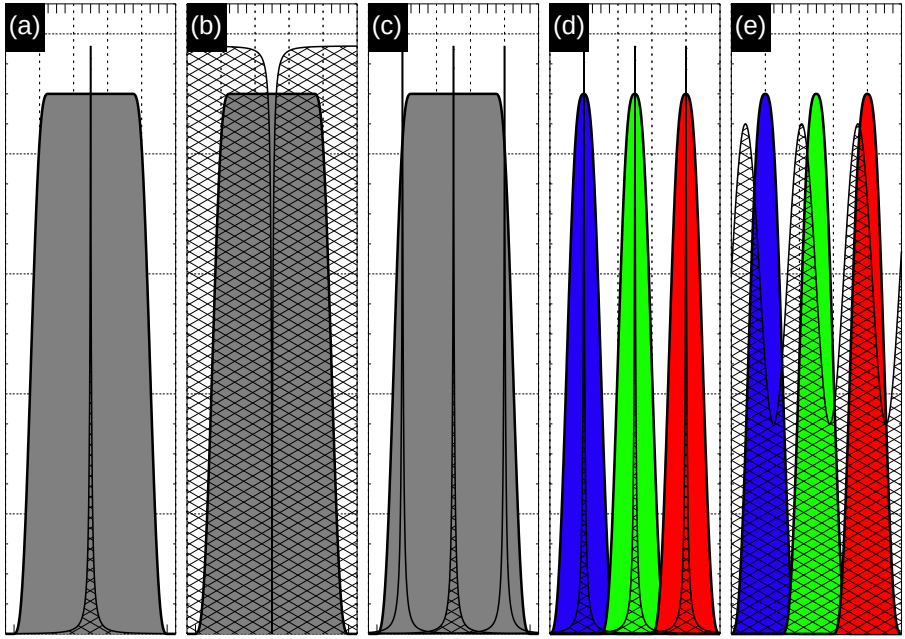

Fig. 19. (a) Broad-band CCD and narrow-band transmission filter, **(b)** broad-band CCD and narrow-band rejection ("notch") filter, **(c)** broad-band CCD and 3 different narrow pass-band transmission filters, **(d)** 3 channel wide-band color CCD and a single transmission filter with 3 narrow pass-bands, **(d)** 3 channel wide-band color CCD and a single modulated transmission filter.

GID
3, 753–823, 2013

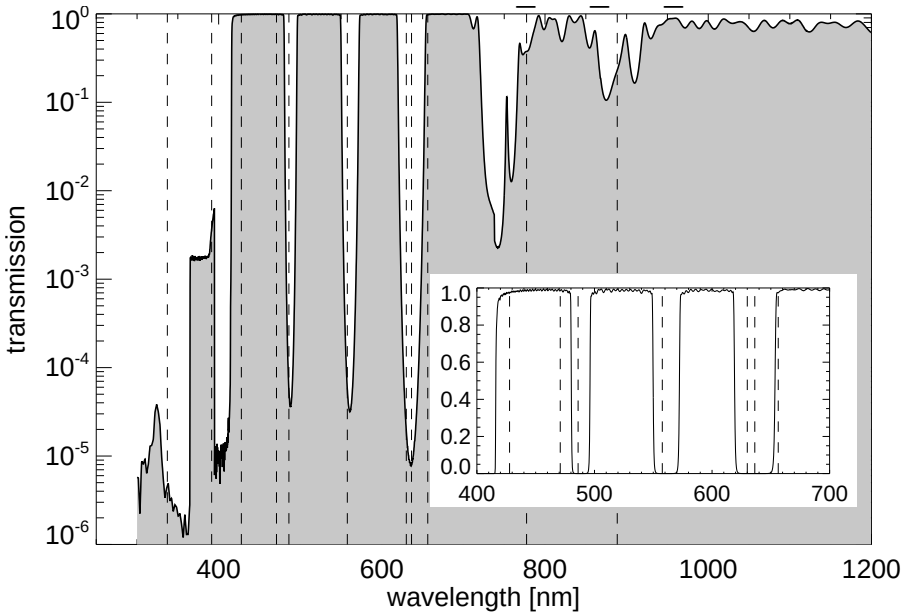

Fig. 20. Spectral transmission for a Semrock NF01-405/488/561/635 multi-notch filter with rejection bands near 405 nm, 488 nm, 561 nm, and 635 nm. Vertical dashed lines correspond to some typical auroral emission wavelengths.

GID
3, 753–823, 2013

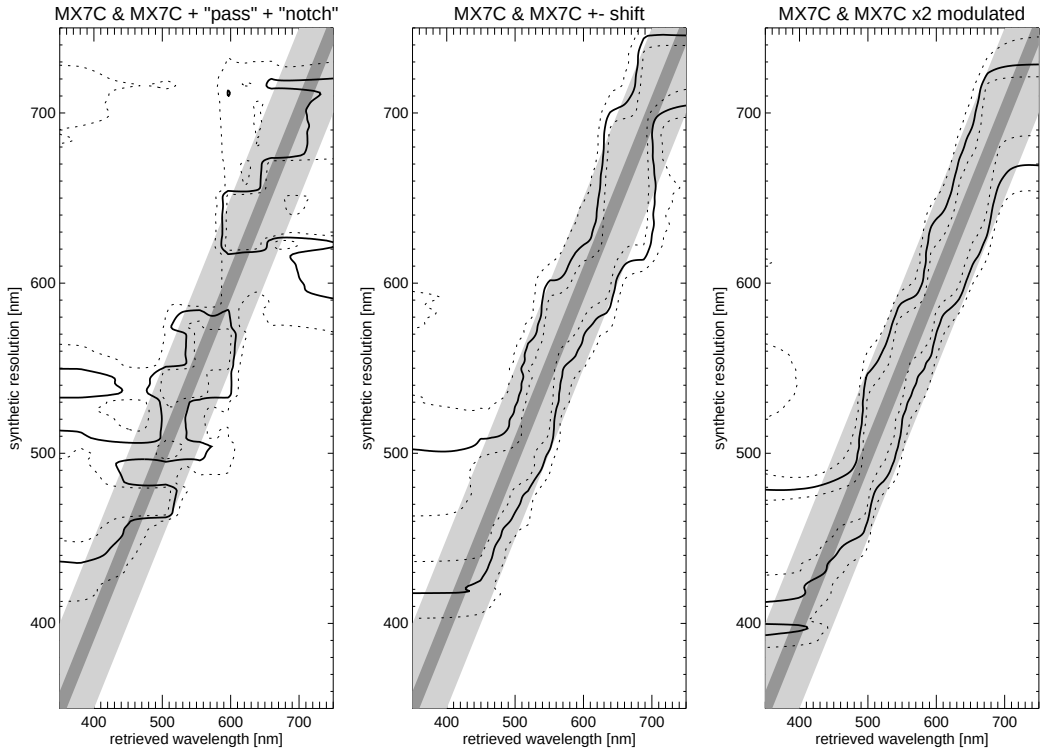

Fig. 21. Backus–Gilbert spectral response analysis for combinations of three color CCDs and filters: **(a)** two different notch filters, **(b)** two wavelength shifts of $\Delta\lambda = \pm 9$ nm, **(c)** two sinusoidal modulations.

GID
3, 753–823, 2013

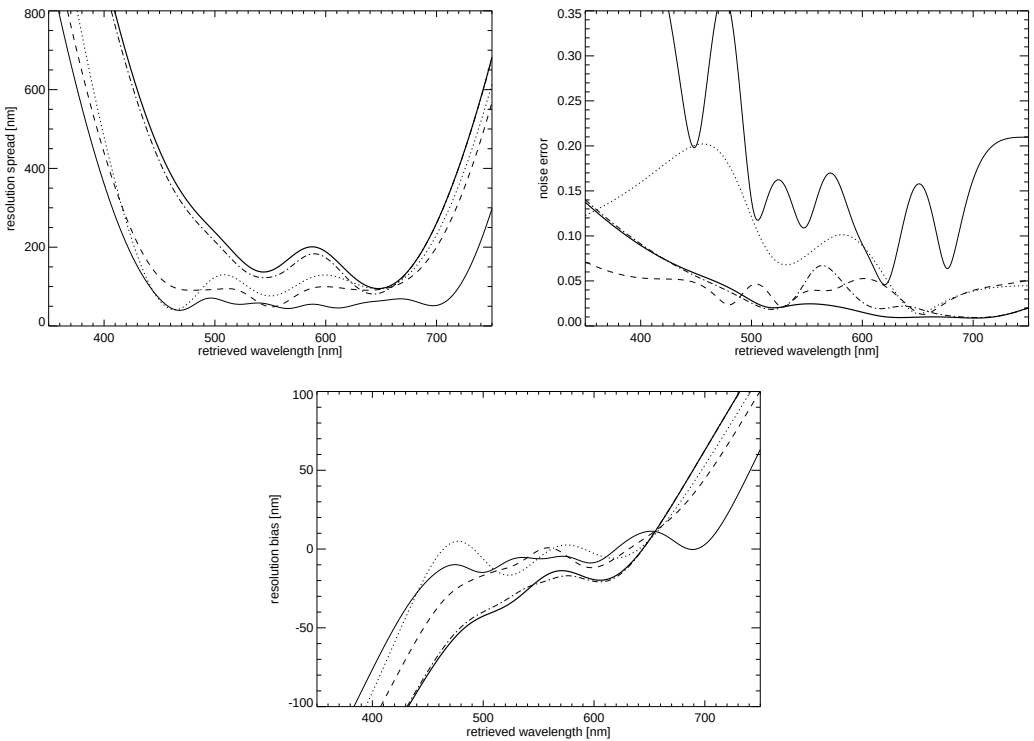

Fig. 22. Retrieval resolution (q_2), noise, and bias (q_3) for MX7C fast (thick solid line), MX7C raw (dotted), H9C/MX7C (dashed), 2 × MX7C with multi-notch filter (dash-dot), 3 × MX7C with two sinusoidal filters (thin solid).

GID
3, 753–823, 2013

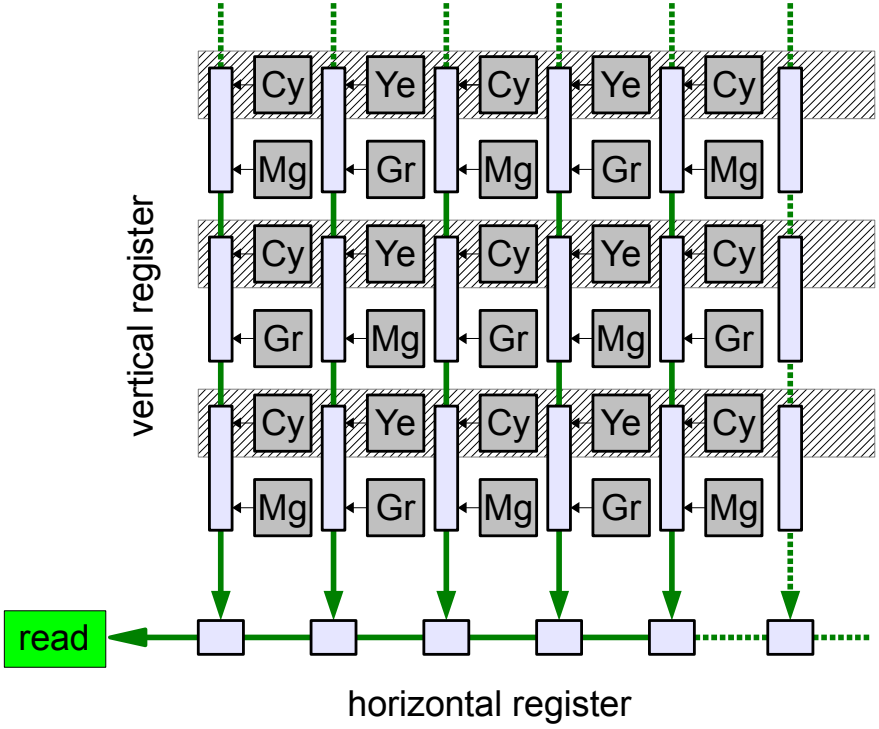

Fig. A1. Interline interlaced CMYG CCD geometry.

GID
3, 753–823, 2013

Wide band color CCD spectral estimation

B. J. Jackel et al.

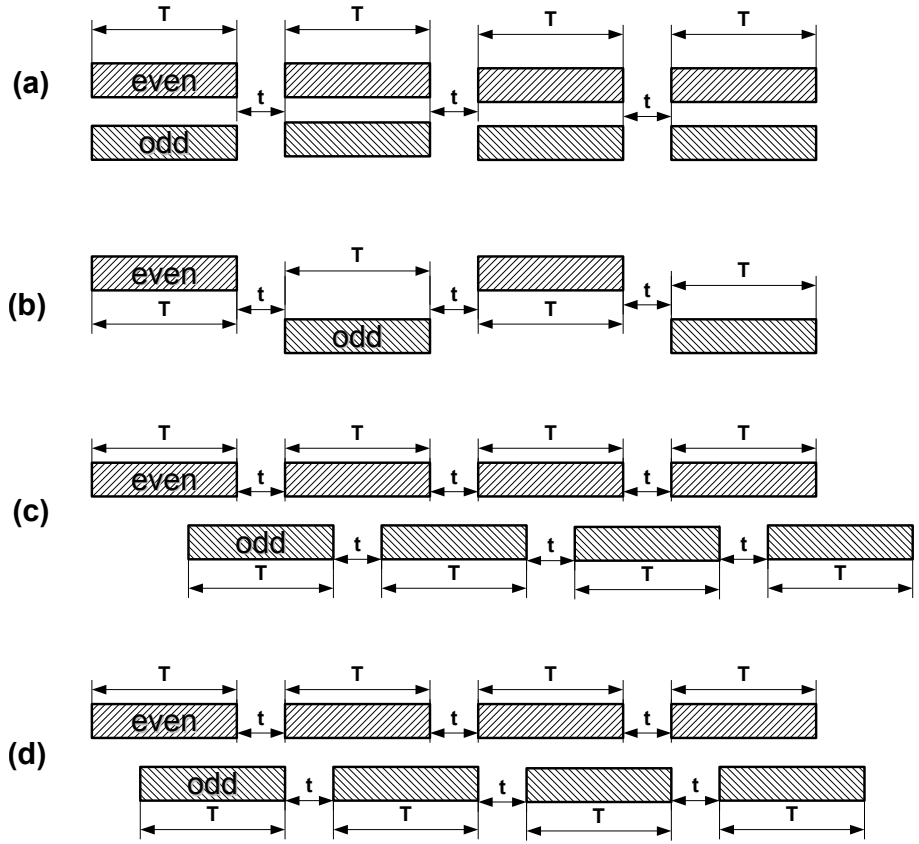

Fig. A2. Timing for interlaced read-out: **(a)** "fast-mode" with combined simultaneous even and odd rows, **(b)** alternating non-overlapping even/odd, **(c)** alternating overlapping offset, **(d)** "pseudo-progressive" alternating minimal offset.

GID
3, 753–823, 2013

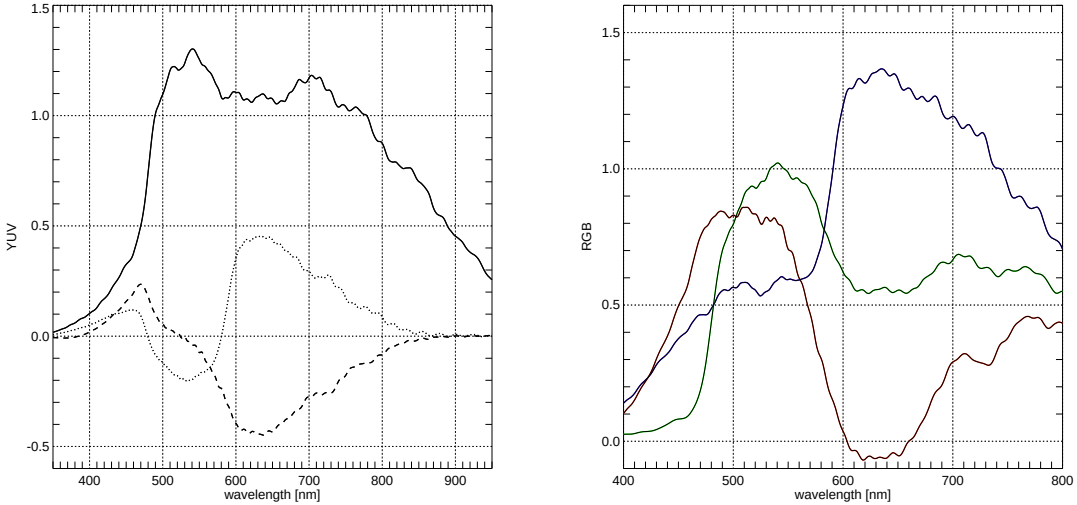

Fig. A3. Fast mode YUV (left) and RGB (right) spectral calibration (no hot filter).

GID
3, 753–823, 2013